HICLASS LADAR Tracking Analysis

Final Report

Prepared for Textron Systems Corp.
201 Lowell St.
Wilmington, MA 01887

Prepared by
Claude Phipps, Ph.D.
Photonic Associates
30 May, 1999
200A Ojo de la Vaca Road
Santa Fe, NM 87505
Phone and FAX 1-505-466-3877
email CRPhipps@aol.com

Table 1. Acronym Glossary

Acronym	Meaning
AEOS	Advanced Electro Optical System (3.67-m aperture telescope)
AO	Adaptive Optics
CCD	Charge Coupled Device
CDLSG	Congressional Debris Language Study Group
CNR	Carrier to Noise Ratio
FOV	Field of View
GEODSS	Ground Based Electro Optical Deep Space Surveillance telescope
GEO	Geostationary Orbit (objects at 36,000 km altitude)
HAX	MIT/LL Haystack Auxiliary Radar at Tyngsboro, MA
HICLASS	HIgh performance CO_2 Ladar Surveillance Sensor
IR	InfraRed
LBD	Laser Beam Director, 0.6-m aperture telescope
JSC	Johnson Spaceflight Center (NASA)
LEO	Low Earth Orbit (objects with mean altitude < 5500km)
LWIR	Long Wavelength InfraRed ($\lambda \geq 10\mu$m spectral region)
MEO	Medium Earth Orbit (objects falling between LEO and GEO)
MIT/LL	Massachusetts Institute of Technology/Lincoln Laboratory
MOA	Memorandum of Agreement
MSSS	Maui Space Surveillance System
PAPA	Commercial name for Lexitek, Inc. detector
ODERACS	Orbital Debris RAdar Calibration Spheres
QE	Quantum Efficiency of a detector
SBR	Signal to Background Ratio
SOR	Air Force Research Laboratory Starfire Optical Range
VIS	Visible Wavelengths (750 nm to 390nm at – 40dB)
XDL	"Times Diffraction-Limited"

1. Executive Summary

In this report, we show that passive, all-optical acquisition of small near-Earth debris targets during twilight and nighttime using existing equipment at MSSS, makes sense. We consider the signal to background ratios involved, and find that a 2.4-m telescope which might be built at MSSS should enable it to acquire cm-size objects with moderately good diffuse reflectivity at 1000km. The 1.6-m telescope at MSSS lacks an adequate FOV for acquisition and is not considered. To minimize expense in setting up a demonstration, a practical solution for a tracking telescope to use in conjunction with the HICLASS ladar might be the 1-m aperture GEODSS site at MSSS.

Active acquisition (for example, acquiring with a ladar) is a bad idea, because of the sparseness of debris targets and the large field of view and consequent high power which must be used in order to generate a reasonable acquisition rate.

In contrast, active tracking with HICLASS and the LBD or, better, the AEOS telescope, should give very good results, better in principle than can be obtained with existing radars. Under the best conditions, using AEOS for both acquisition and in conjunction with HICLASS for tracking, it should be possible to acquire and track 100 times as many targets per hour at 1000km range, these targets being twice as small, as with radar. Considering tracking by itself, AEOS/HICLASS should see 7-

times-smaller targets (1.2-mm). If a target is acquired, it can certainly be tracked. Handoff between acquisition and tracking is considered in some detail.

We sketch a test program which might involve NASA's cooperation in launching test targets in low Earth orbit (LEO) for initial demonstration.

The long wavelength, high peak power and near-photon-counting performance of HICLASS and its receiver combined with the cold, high altitude Maui site are responsible for the good results obtained.

The concept of using the Earth's own radiation to illuminate targets for all night viewing, is considered.

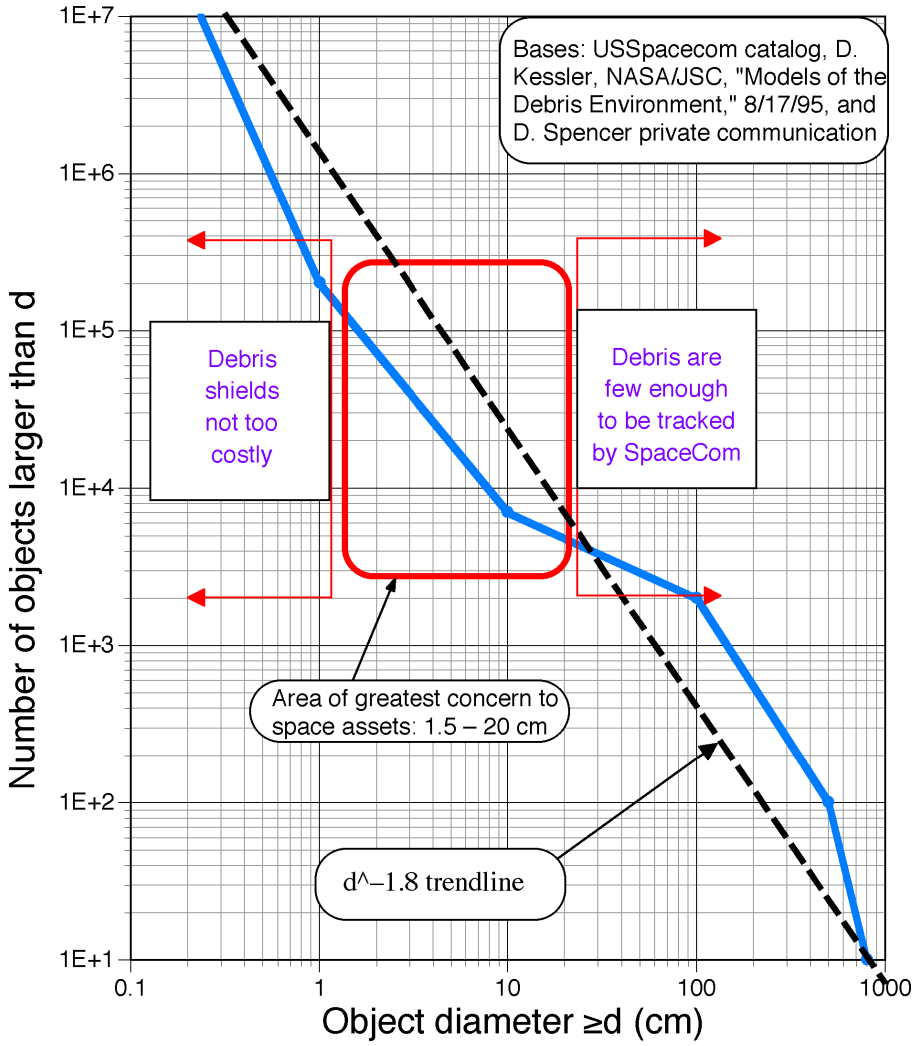

Figure 1. Total Number of Low-Earth-Orbit Debris

Table 2: Kinetic energy of objects at high closing velocity

At 12 km/s, a:	Packs as much energy as:
5-mm dia. paint flake	12-pound barbell dropped from 2nd story
2-mm "BB" pellet	100-pound anvil dropped from 7th story
Penny	Volkswagen hitting a brick wall at 50mph

2. Background

2.1 Manmade Debris in LEO

There are presently 110k to 150k LEO debris objects between 1 and 10-cm diameter. (Figure 1, Table 3) [Hogge and Spencer, 1998; Phipps *et al* 1996]. Debris density peaks in the popular 700–1100km altitude band, in which lifetime is 10yr to >10kyr, depending on size, area/mass ratio and altitude.

The total mass of manmade orbital debris within 2000km of the Earth's surface is about 2,000 tonnes [OSTP 1995].

Because the parent objects were launched at many different inclinations to the Equator, the closing velocity between debris and an object in orbit can be 12km/s.

The debris threat arises from the combination of flux and kinetic energy. Table 2 illustrates the tremendous kinetic energy possessed by objects as small as paint flakes at 12km/s, and Table 3 indicates the approximate number and flux [Stansbery 1996].

The 1–10-cm size range is especially important because, below 1cm, mechanical shielding of spacecraft is not prohibitively expensive and,

above 10 cm, the debris flux is so much smaller (dropping like $d^{2.5}$) that the threat is manageable.

The Table shows that an object or fleet in the highest band with cross-sectional area 10,000 m^2 will be hit once a year. One can equally easily interpret this number to say that a single satellite with 10m^2 cross-section will be hit once per millennium, or that the Teledesic fleet, with projected area of about 20,000 m^2 will be hit twice a year, and that these hits will be fatal to 2-3 satellites during that program.

Table 3: Number and Flux of 1 – 10-cm Debris

Altitude Band (km)	Number at or below band	Flux in band (m^{-2} yr^{-1})
700-1100	150k	1E-4
400-600	40k	2E-6
300	10 (Test targets, proposed)	-----

Even the lower flux in the 400km band is significant for the NASA Space Station.

2.2 Existing Capability

The US Air Force has an interest in improving its capability to track (but not rigorously catalog) orbital debris. That interest led to the formation of the *ad hoc* USAF Congressional Debris Language Study Group (CDLSG) [Hogge & Spencer, 1998]. The CDLSG report identified seven "critical shortfalls" in the U.S. capability to do better debris tracking and possibly partial cataloging in the following areas:

(1) Orbit determination

(2) Atmospheric density measurements

(3) Predicting atmospheric drag on satellites

(4) Radar system upgrades

(5) Correlation of radar and optical cross-section measurements and other optical properties of debris

(6) Demonstrated hand-off

(7) Demonstrated ladar capability for sampling debris flux, and tracking debris.

One of its major conclusions was that we should "improve our understanding and monitoring of the debris environment through an appropriate mix of measurements and simulations."

This report is a first attempt to meet this request.

CDLSG identified HICLASS as a ladar which can operate as part of a network of sensors to detect and track orbital debris, and that its capability could be increased by putting it on a larger telescope. It can provide high precision metrics, images, sizes, and even shape and orientation for some debris objects.

It was claimed that existing GEODSS systems have limiting magnitude of visual magnitude m_v =12 in chase mode, limiting these to acquiring 12-cm solar-illuminated objects at 500km range, during twilight. This figure can be improved by upgrading the focal plane arrays, frame subtraction, etc.

Current NASA models for 1–10-cm debris are largely based on data obtained with the Haystack or HAX radars at MIT Lincoln Laboratory. Haystack is able to make from 0.1 - 1 detections per hour and detect a 1-cm sphere at 1000km. It can also measure polarized and depolarized reflectance and has detected the spin rate of a number of objects.

However, radar cross-sections are not as useful as optical ones. There is a potentially large subset of objects which have low visibility to radar but are optically bright, such as multilayer insulation. Discovering that there are a lot of these could substantially increase the flux of threat debris relative to present models. On the other hand, observers have noted optical and radar populations in the d<20cm range with σ_{radar}:$\sigma_{optical} \Rightarrow 2$. Optical characterization of the objects will help determine what they are

and, thus, area to mass ratios, actual size, etc. Previously, only NASA's ODERACS campaign (using orbiting radar calibration spheres) was able to do this.

Smaller objects at the lower altitudes show large and unpredictable nongravitational orbit perturbations due to atmospheric drag and solar wind, making it extremely difficult to reacquire the smaller objects on the next pass after discovery. Without accurate range information, which can be provided by HICLASS, optical tracking is ineffective in determining orbital ephemerides, which are critical for predicting subsequent apparitions [Appendix IV].

The HICLASS kW-class CO_2 ladar is a critical ingredient for addressing 6 of the 7 shortfalls as well as other problems listed above.

3. Outline of Report

The quantitative capabilities of HICLASS as a debris tracker, operating with telescopes presently at MSSS, will be determined. Examples of applications are: accurately determining debris orbits with sufficient precision to give information on atmospheric density variations in near real-time, helping to correlate optical to radar cross-sections, determining the composition of debris and finding debris missed by radar.

Techniques developed for NASA in Phipps, 1997, Campbell, 1996 and Phipps, *et al* 1996 coupled with data from Stansbery, *et al* 1996 and Kessler, *et al* 1996 will be applied to this assessment.

The areas we address are:

- Logical options for acquisition and tracking
- Where HICLASS could be useful within the present space debris network
- Analysis of acquisition and tracking using various devices
- Analysis of a novel idea for acquisition using Earth's radiated LWIR energy at nighttime to illuminate targets
- Recommendations concerning demonstrations that can be done using HICLASS and other equipment at MSSS.

These are complex problems which cannot be covered fully at the level of effort represented here. For that reason, we discuss future work [§11].

Appendices to the main report treat:

- Acquisition rate calculations
- Target albedo
- Arrays
- Orbits, apparent motion and atmospheric drag

Table 4: Physical Symbols, Constants, Units and Conversions

[typical usage in this report highlighted]

Quantity	Symbol	Practical cgs	SI
Average value of quantity	< >	— — —	— — —
Spectral brightness (e.g., of background)	B_λ	**W cm^{-2}sr^{-1}μm^{-1}**, x1E10=	Wm^{-2}sr^{-1}m^{-1}
Speed of light	c	3E10 cm/s	3E8 m/s
Decibel	dB	10x$\log_{10}$ of ratio	**----**
Diameter of target	d	**cm**, x 1E-2 =	m
Diameter of illuminated area or field of view at target range	d_s	cm, x 1E-2 =	**m**
Minimum value of d_s set by diffraction	d_{sDL}	cm, x 1E-2 =	**m**
Diameter of aperture on the ground	D_b	cm, x1E-2 =	**m**
Shorthand for "10^"	E	— — —	— — —
Repetition frequency	f	s $^{-1}$	s $^{-1}$
Target orbit altitude	h	cm, x 1E-5	**km**
Quantum efficiency, p.e. per photon	η_e	— — —	— — —
Planck constant	***h***	6.626E-34 J-s	6.626E-34 J-s
Spectral intensity of the sun at λ	I_λ	**W cm^{-2}μm^{-1}**, x 1E4 =	W m^{-2}μm^{-1}
Boltzmann constant	k	1.381E-23 J/K	1.381E-23 J/K
Beam quality number	m^2	— — —	— — —
Visual magnitude = –2.5 log brightness	m_v	— — —	— — —
Laser frequency c/λ	ν	s^{-1}	s^{-1}
Number of targets	N	— — —	— — —
Number of photoelectrons per pixel	N_{pe}	— — —	— — —
Power = fW	P	W	W
Array element size (qxq)	q	— — —	— — —
Out-of-band rejection (heterodyne rcvr.)	ρ	— — —	— — —
Bond albedo (diffuse reflectivity into π)	R	— — —	— — —
Earth radius	R_E	cm, x 1E-5	**km**
Signal-to-background ratio	SBR	— — —	— — —
Stefan Boltzmann constant	σ_{SB}	**5.67E-12 W cm^{-2}K^{-4}**	5.67E-8Wm^{-2}K^{-4}
Source to target optical transmission	T	— — —	— — —
Temperature	***T***	K	K
Orbit velocity	v_o	cm/s, x 1E-5 =	**km/s**
Geocentric orbit velocity	$\mathbf{v}_o$	rad/s	
Velocity of the FOV while slewing	v_s	cm/s, x 1E-5	**km/s**
Geocentric slewing velocity	$\mathbf{v}_s$	rad/s	
Laser pulse energy	W	J	J
Tracking accuracy $\perp$ laser beam	Δx, Δy	cm, x 1E-2	**m**
Range tracking accuracy	Δz	cm, x 1E-2	**m**
Target range	z	cm, x 1E-5	**km**

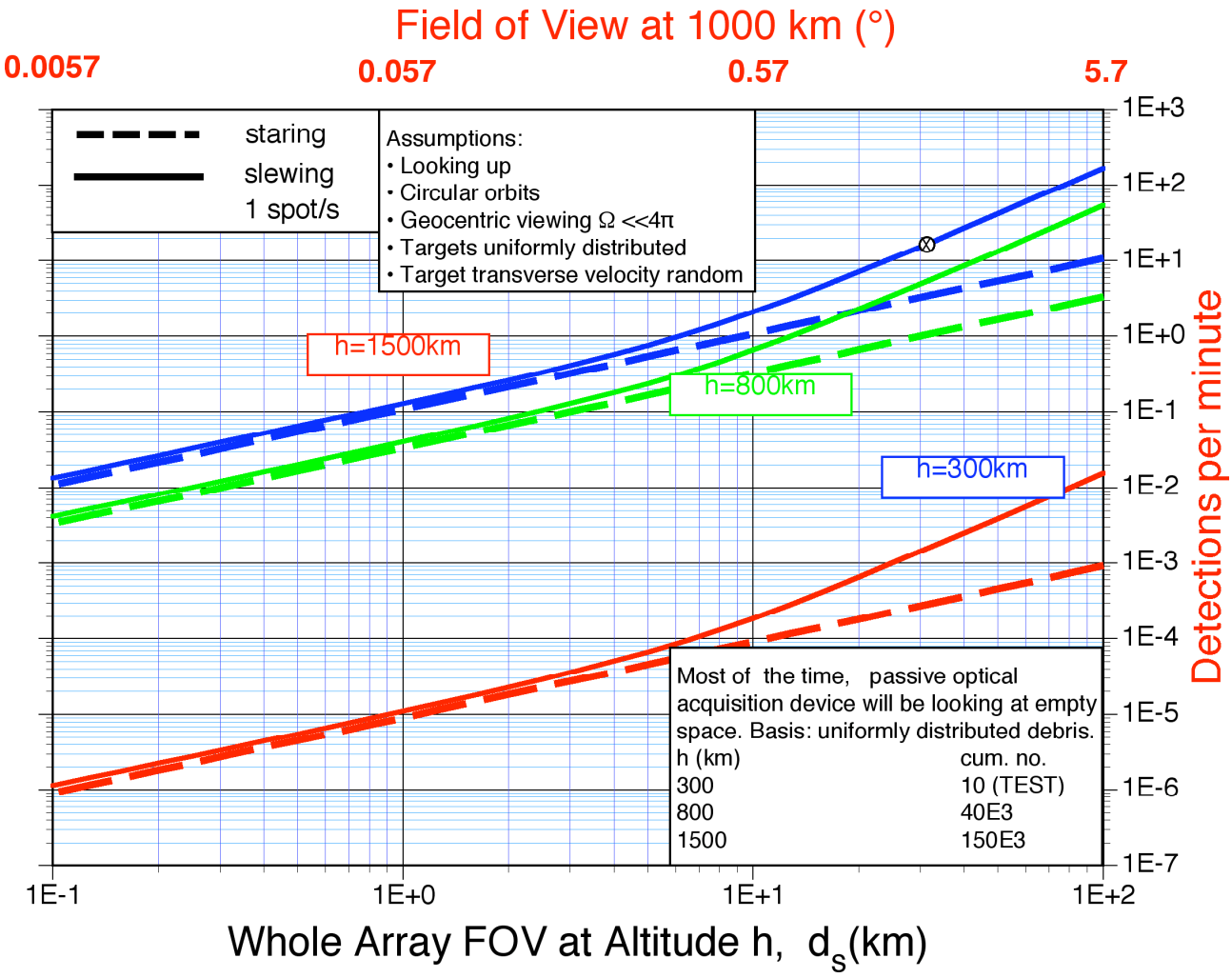

Figure 2. Acquisition rate vs. diameter of the field of view (FOV) at range for the entire acquisition array, assuming uniform target distribution. The advantages of slewing the FOV at one spot per second [solid lines], compared to staring [dashed lines], are illustrated. The dashed lines make it clear that acquisition rate is linearly proportional to the FOV diameter rather than its area. Higher slew rate would give higher acquisition rate. [see Appendix I]. Assumptions are listed in the boxes.

The point of the graph is that the necessary FOV of the entire acquisition array can be considered as determined by the desired acquisition rate [Eq.A1.12c]. The "meatball" on the 1500km altitude plot shows that, for example, to acquire 17 objects per hour [12k objects per year during twilight conditions with 65% clear weather], we need an FOV = 32 mrad or 1.8 degrees. For comparison, Haystack, with a 1 mrad FOV, should on average acquire an object every 5.5 hours. "Clustering" (isolated density concentrations) will give higher rates.

4 Passive Visible Optical Acquisition of 1–10-cm Debris in LEO

4.1 Field of view of the sensor array controls target acquisition rate

Acquisition and Tracking are very different functions. The number of objects and the acquisition sensor field of view control the acquisition rate. We assume a uniform distribution (a worst case for acquisition, probably pessimistic by a factor of 5 relative to the best case because of clustering). Figure

2 shows the relationship between field of view and acquisition rate. The inset box in Figure 2 shows the cumulative number of targets assumed in the bands topped by 800 and 1500 km altitude to generate the acquisition rates shown. Also assumed in the box are 10 artificial targets with low area/mass ratio for long lifetime at low altitude which it is proposed be injected at about 300km using NASA assistance, to demonstrate target acquisition and tracking. NASA released similar targets in the ODERACS campaign.

In the example illustrated in Figure 2, a field of view of 1.8° will give, on the average, 17 acquisitions per hour (one per 3.5 minutes). This figure was chosen for study because it is a practical data rate considering the expense of operation time. It also corresponds to 12k acquisitions per year during dusk with 65% clear weather, a rate at which acquiring all the debris in Table 2 will take 15 years.

The 2-D model we developed to generate the curves in Figure 2, as well as the notations in the boxes, are explained in Appendix I.

4.2 FOV of a single acquisition array pixel is set by SBR

Background spectral brightness that we use for this analysis is shown in Table 5.

Table 5. Sky background for various conditions
[Allen, 1973; Wolfe & Zissis, 1978; Reilly, 1996]

Site/Time of Day, Line of Sight	Center Spectrum λ	Spectral Brightness B_λ ($\mu Wcm^{-2}sr^{-1}\mu m^{-1}$)	Example: Photons/s onto 1 pixel with FOV = 13μrad via a D_b=3.67m collection aperture at $\lambda \pm 0.2\mu$m
Typical/Clear Twilight, Vertical	550 nm	0.05	3.9E5
Typical/Clear Night, No Moon, Vertical	550 nm	0.0005	3.9E3
Typical/Clear Night, Moon, Vertical	550 nm	0.005	3.9E4
Typical/Clear Night, Vertical	11.2 μm	200	7.9E7
Typical/Clear Night, 30° from Vertical	11.2 μm	400	1.6E8
MSSS/Best, Cold Night (est.), Vertical	11.2 μm	20	7.9E6

13μrad FOV is chosen in the last column of Table 5 because it is the full-angle diffraction-limited divergence corresponding to a 10 cm turbulence-cell at 0.55μm, as well as that of a 1.8XDL 3.67-m aperture at 11.2μm.

Regarding column 3 of Table 5,: the etendue theorem guarantees that it doesn't matter whether we consider the area of the diffuse source times the solid angle subtended by the receiver as viewed from the source, or the area of the receiver times the solid angle subtended by the extended diffuse source as viewed from the receiver. So, for viewing sky background with a 367-cm aperture (column 4, Table 5):

$$\text{Photon rate} = B_\lambda * \pi d\theta^2/4 * 0.2 * \pi * 367^2/4 \qquad [1]$$

Therefore, with passive solar illumination, SBR is determined by the simple relationship:

$$SBR = \frac{R\, I_\lambda}{\pi\, B_\lambda}\left(\frac{d}{d_{sp}}\right)^2 . \qquad [2]$$

[see Appendix II for a discussion of diffuse reflectivity, and the appropriate values to use in various cases treated in this analysis].

To calculate SBR for passive optical acquisition, the remaining ingredient is the spectral intensity of the illumination source, given in Table 6. Eqn. [3] looks different from the normal radar-type equations because we have chosen to parameterize d_s, the diameter of the FOV at range, rather than range, for greater simplicity.

That is to say, it is more flexible to think of d_s as a free variable (so long as it is not less than permitted by diffraction) rather than simply being controlled by viewing aperture size D_b and turbulence transverse coherence length.

If the analysis shows we need this flexibility, we would then modify the acquisition instrument to accommodate a small amount of adjustable "zoom" so that $d_s \geq d_{sDL}$.

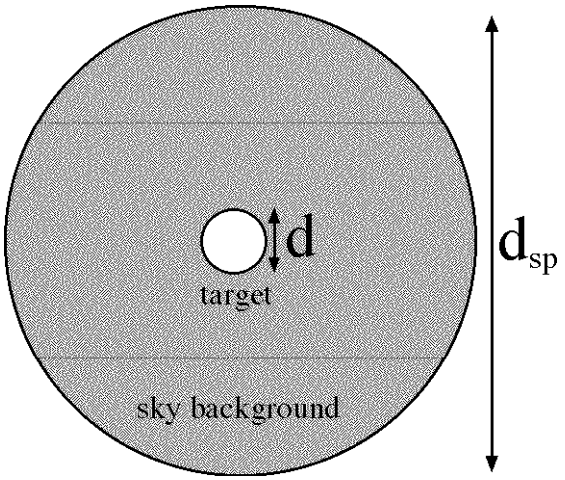

Figure 3. In Eq.[3]. d_{sp} is footprint of one pixel at range z

Table 6: Spectral intensity of sources in near-Earth space [Allen, 1973]

Source ⇒	Sun	Earth
I_λ (W cm$^{-2}\mu$m^{-1})	0.1	0.006
At λ	typ mid-VIS	IR, 11μm

Given the above, and that we express SBR in terms of a target diffuse reflectivity R into π sterrad (analogous to Bond albedo), RI_λ and background B_λ have the same dimensions and the size of the receiving aperture is irrelevant for SBR so long as it can make a spot as small as d_{sp}.

The ratio of the two FOV's gives the array size in elements q:

q = array FOV/element FOV [3]

4.3 Adequate SBR and N_{pe} define the acquisition problem

Although we may slew the detector in acquisition mode, we cannot utilize the SBR benefit that accrues from tracking targets, since the paths of the objects we are trying to find are not known *a priori*. Tracking is a much better case, since photons can be integrated up on one pixel or one bin. For this reason, we have to consider N_{pe} on one pixel during a *target streak* across the array [hence, v_o appears in the denominator of the expression for N_{pe} in the inset, Figure 4B].

The above considerations are combined in the two equations shown in the inset of Figures 4A and 4B for SBR and N_{pe}. Because of the complexity of the parameter space involved, and to show how the chart works, we have identified two possible values of the product $D_b d\sqrt{R}$ in Figure 4B which produce (A) N_{pe} = 1000, (B) N_{pe} = 100 and (C) N_{pe} = 15 photons per pixel during a target streak, respectively. For each choice, multiple choices of debris size d and time of day (night or twilight) are possible, each giving different SBR. Selected examples of these are listed in Table 7. In Figures 4, as in Figure 3, d_{sp} is the spot size at range which a single pixel in the acquisition focal plane array maps onto.

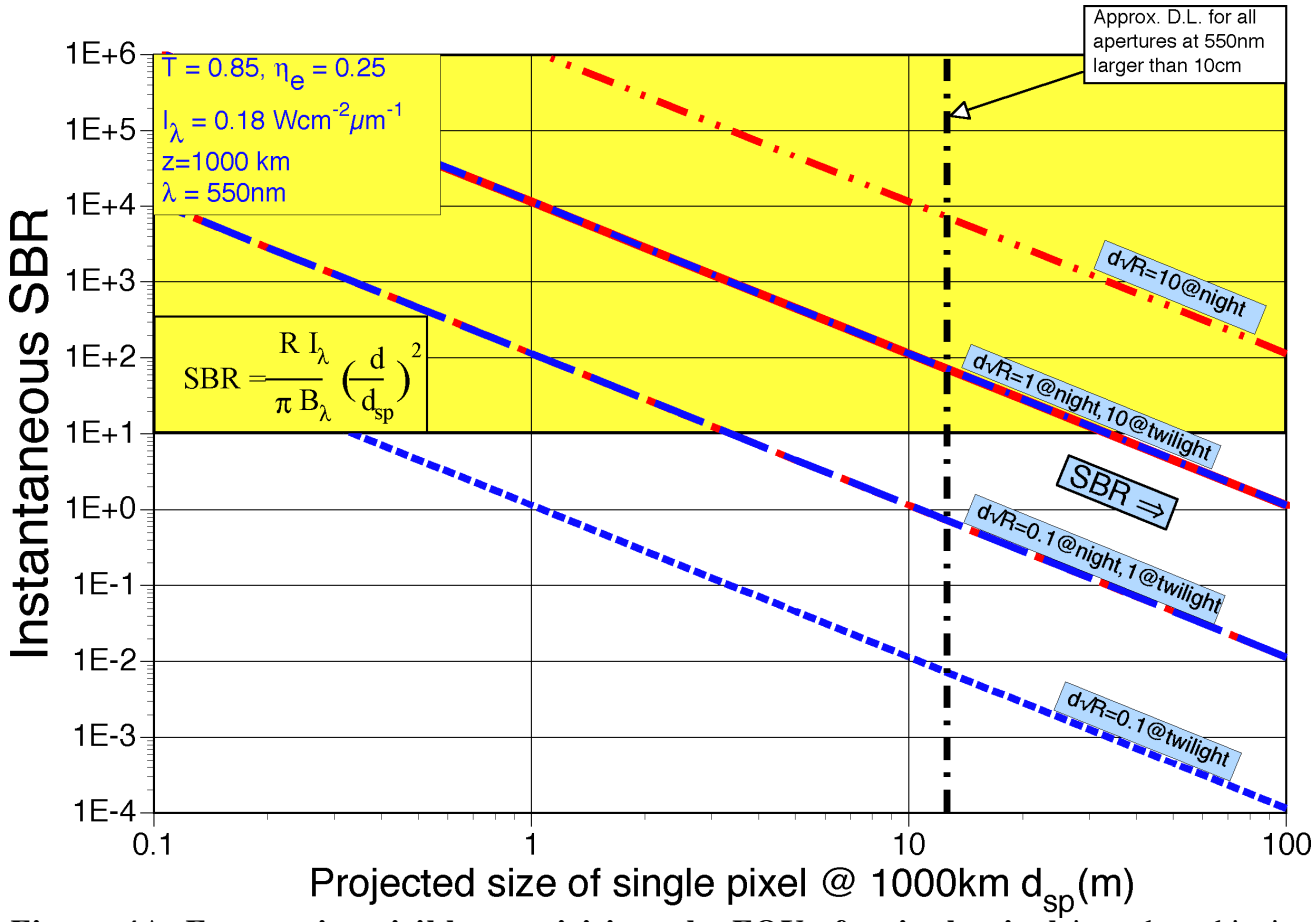

Figure 4A. For passive visible acquisition, the FOV of a single pixel is set by achieving the desired SBR. This Figure shows SBR vs. spot size d_{sp} in space which maps onto one pixel on the array. The case shown is computed for solar illumination in the 0.2-μm window around 0.55μm. Atmospheric transmission T = 0.85, range is 1000km. Horizontal axis is mrad when z = 1000km. The vertical black dashed line at 13μrad is the FOV for any visible wavelength aperture larger than 10 cm, for uncorrected turbulence (no AO). The gold area is the desirable operating region. Plots of SBR slope downward to the right. The parameter for these (shown in boxes) is d√R. Plots overlap in two cases where a factor-of-10 change in d√R matches an equal change in background between night and twilight. See Figure 4B following for operating points. For each of these, the consequences on SBR of picking a particular aperture size D_b [the only remaining free variable] are summarized in Table 7. Criteria for assessing these SBR's are given following the Table.

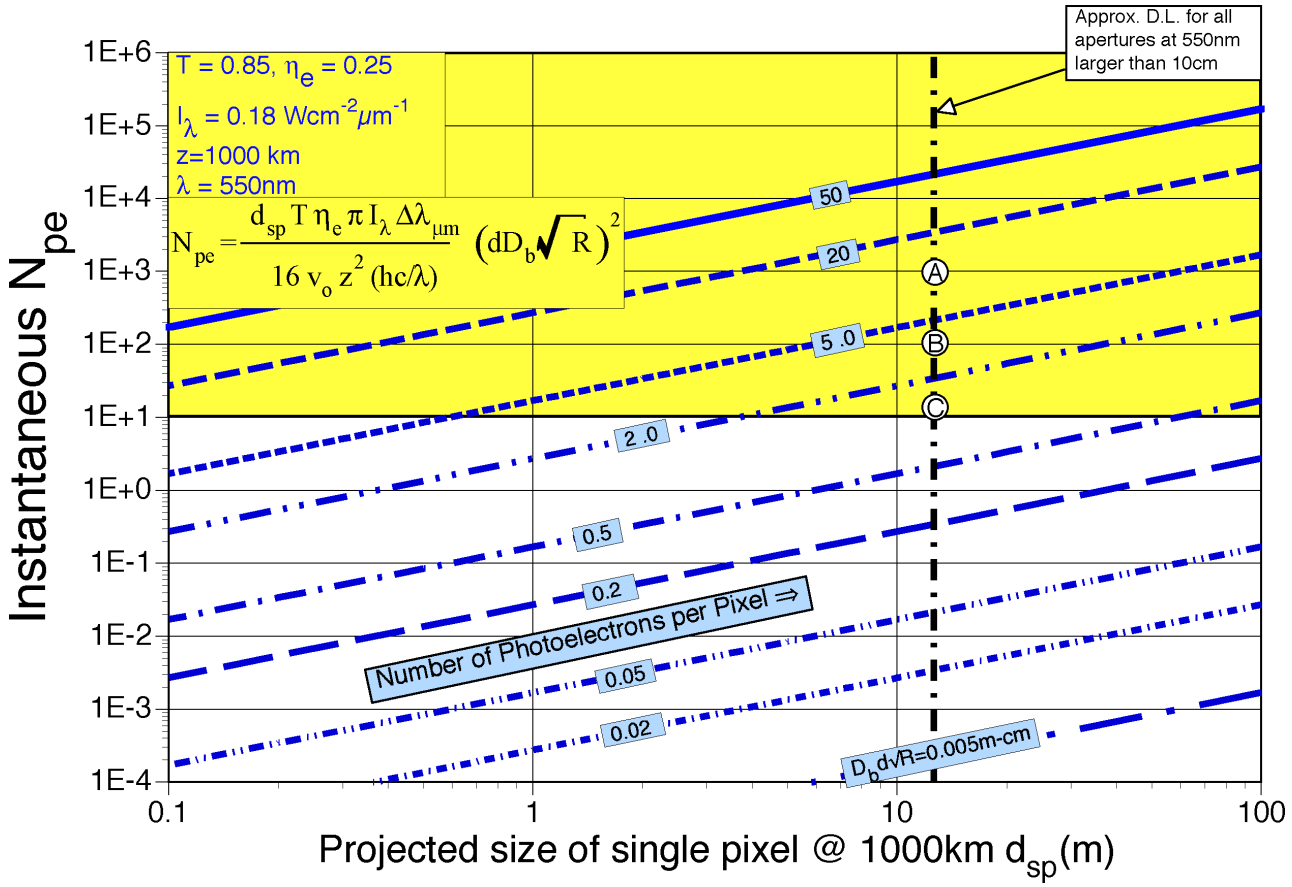

Figure 4B. For passive visible acquisition, an adequate number of photo-electrons must be obtained simultaneously with the SBR's shown in Figure 4A. This Figure shows number of photo-electrons per single pixel N_{pe} in staring mode vs. spot size in space d_{sp} which maps onto one pixel. Because the acquisition sensor is staring, orbital velocity v_o enters into N_{pe}. Quantum efficiency η_e is 25%. We picked such a small QE for this example to match the Lexitek PAPA device (Appendix III). Factor-of-3 greater QE and N_{pe} are possible. Horizontal axis is mrad when z = 1000km. The vertical black dashed line at 13μrad is the FOV for any visible wavelength aperture larger than 10 cm, which is the size of a VIS-λ turbulence cell (no AO). The gold area is the desirable operating region. Plots of N_{pe} are in light blue and slope upward to the right. The parameter for these is $D_b d\sqrt{R}$ (values shown in boxes) with units of meter-cm/√sterradian. This is the product of receiving aperture diameter in meters, debris diameter in cm and the square root of debris diffuse reflectivity R into π sterradians. As in Figure 4A, three possible operating points are shown which illustrate (A) N_{pe} = 1000, (B) N_{pe} = 100 and (C) N_{pe} = 15. Values obtained for N_{pe} are listed in Table 7.

Table 7: Possible operating points (A,B,C) in Figs. 4A & 4B with selected values D_b & SBR [FOV = 13μrad is assumed]

Figs. 4 Meatball	FOV, μrad	$D_b d\sqrt{R}$	N_{pe} /pixel	$d\sqrt{R}$	debris d (cm)	Aperture D_b(m)	R	SBR (night)	SBR (twilight)
A	13	10	1000	10	20	1.00	0.25	140	14
A	13	10	1000	4.1	8.2	2.4	0.25	1350	135
A	13	10	1000	2.7	5.4	3.67	0.25	590	59
A	13	10	1000	1.6	3.1	6.4	0.25	200	20
B	13	3.2	100	3.2	6.4	1.00	0.25	1500	150
B	13	3.2	100	1.3	2.6	2.4	0.25	140	14
B	13	3.2	100	0.87	1.7	3.67	0.25	60	6
B	13	3.2	100	0.50	1.0	6.4	0.25	20	2
C	13	1.2	15	1.6	2.4	1.00	0.25	210	21
C	13	1.2	15	0.50	1.0	2.4	0.25	20	2
C	13	1.2	15	0.32	0.46	3.67	0.50	8	0.8
C	13	1.2	15	0.32	0.32	3.67	1	8	0.8
C	13	1.2	15	0.33	0.19	3.67	π	9	0.9

4.4 Criteria for Acquisition

We apply the following two criteria to find solutions for visible solar-illuminated debris acquisition using modern CCD arrays in Table 7 and Figures 4:

Acquisition Criterion 1. Robust false alarm rate requires SBR ≈ 10.

Acquisition Criterion 2. Robust carrier-to-noise ratio (CNR>12dB) requires $N_{pe} \geq 15$.

If we apply both criteria, we see that there are some tricky tradeoffs in choosing parameters, since there are two limiting conditions, either one of which can become dominant depending on our choices.

This interaction among choices is illustrated in Table 8.

Table 8. Illustrating tradeoffs in choosing parameters to meet limiting conditions

[550nm, 1000 km, 13μrad FOV, 25% QE. If $N_{pe} \geq 15$, $D_b d\sqrt{R} \geq 1.2$ m-cm/$\sqrt{}$sterrad
If SBR ≥10, $d\sqrt{R} \geq 0.32$ cm/$\sqrt{}$sterrad (night) or $d\sqrt{R} \geq 1.00$ cm/$\sqrt{}$sterrad (twilight)

Limiting Condition in Blue

Results in Red

Night:

Case	D_b (m)	SBR	$\therefore d\sqrt{R}$	$\therefore D_b d\sqrt{R}$	& N_{pe}
1	3.67	10	0.32	1.2	15
Case	D_b (m)	N_{pe}	$\therefore D_b d\sqrt{R}$	$\therefore d\sqrt{R}$	& SBR
2	2.4	15	1.2	0.50	20

R	d(cm)
0.10	1.0
0.25	0.6
1.00	0.3

R	d(cm)
0.10	1.6
0.25	1.0
1.00	0.5

Twilight:

Case	D_b (m)	SBR	$\therefore d\sqrt{R}$	$\therefore D_b d\sqrt{R}$	& N_{pe}
3	3.67	10	1.00	3.7	150
Case	D_b (m)	SBR	$\therefore d\sqrt{R}$	$\therefore D_b d\sqrt{R}$	& N_{pe}
4	2.4	10	1.00	2.4	60

R	d(cm)
0.10	3.2
0.25	2.0
1.00	1.0

Case 1-4 are different from cases A,B,C in Figures 4A and 4B.

Cases 1,2: In going from 3.7 m aperture to 2.4 m aperture at night, the limiting condition switches from achieving adequate SBR to achieving adequate photon count on a pixel. The conclusions in the two cases are that $d\sqrt{R}$ should be at least 0.32 and 0.50, respectively and these products are shown in the two boxes at the right for 3 assumptions about albedo, or that 1-cm objects can be seen down to albedos of 10% and 25% respectively.

Cases 3,4: In going from 3.7 m aperture to 2.4 m aperture at local twilight, the limiting condition stays the same: achieving adequate SBR, rather than achieving adequate photon count on a pixel. The conclusions in the two cases are therefore the same: $d\sqrt{R}$ should be 1.0, and 1-cm objects can be seen only for albedos of 100%. For more likely albedos, only 2–3-cm objects can be seen because of the greater background at twilight. It doesn't matter what size the mirror is, between the two choices.

It should be emphasized that R can be >1 or even >>1 as for example for a reflective metal plate [Appendix II].

The particular values of interest for acquisition at MSSS are D_b = 3.67m (AEOS) and 2.4m, a hypothetical telescope which could be built relatively inexpensively [Pohle 1998].

Table 9: Minimum acquired targets meeting criteria 1) and 2) above staring at 550nm, 1000 km, 13μrad FOV, and 25% QE, for local twilight and night.

D_b(m)	R	d (cm)	Limit	Condition
3.67	0.02	8.0	SBR	Twilight
3.67	0.10	3.6	SBR	Twilight
3.67	0.25	0.72	SBR	Night
3.67	1	0.36	SBR	Night
3.67	π	0.20	SBR	Night
2.4	0.02	8.0	SBR	Twilight
2.4	0.10	3.6	SBR	Twilight
2.4	0.25	0.72	N_{pe}	Night
2.4	1	0.36	N_{pe}	Night
2.4	π	0.20	N_{pe}	Night
1.00	0.02	8.6	N_{pe}	Twilight
1.00	0.10	3.9	N_{pe}	Twilight
1.00	0.25	2.5	N_{pe}	Night
1.00	1	1.2	N_{pe}	Night
1.00	π	0.65	N_{pe}	Night

By repeating the Table 8 procedure several times for a broader range of parameters, we reach the conclusions for acquisition summarized in Table 9. The mirror size 1.0 m matches the aperture of GEODSS at MSSS, which we believe to be a good candidate for an acquisition demonstration. Its present performance will not match that shown here without a high performance focal plane array and gating or frame subtraction [§4.5].

Debris which reflect incident sunlight into no more than 1 sterradian ($R \geq \pi$) can be acquired just before dawn or just after nighttime twilight down to 2 mm in size. These may not be all that rare, but that will not be known until we do the proposed tests.

Objects with what we regard to be a conservative diffuse reflectivity ($R = 0.25$ into π sterrad but not beyond that angle) can be acquired down to 7.2 mm in size.

It is clear that decreasing acquisition instrument aperture diameter begins to cause performance penalties at 1 m, for the brighter objects where SBR is not a problem but sheer number of photons collected is.

We also conclude that, with an FOV of 13μrad and earlier results, Eqn. [3] gives $q = 32\text{mrad}/13\mu\text{rad} \approx 2048$, or 2048x2048 elements per acquisition array.

4.5 CCD Arrays should be gated, or image subtraction employed

In order to achieve the results quoted above, the acquisition array must be gated for an interval

$$\Delta t = d_{sp}/v_o. \qquad [4]$$

Background photons add up for the entire frame integration time Δt_f, while signal photons do so only during the interval Δt. If these times are not equal, the SBR's we have been quoting are optimistic by the ratio $\Delta t_f/\Delta t$. By repetitively gating the array for the interval $\Delta t \approx 1.5$ms and reading it out in some fashion, we avoid this problem. For a CCD array, the result is a series of dots representing the target, rather than a streak.

An alternative which may achieve the same results, but which is not studied in this report, is successive frame subtraction with interval given by Eq. [4]. There are detailed differences between the approaches having to do with atmospheric scintillation which need to be studied.

There are several ways to do this. Some are listed following, and others are discussed in Appendix III.

1. The most obvious solution is to install a fast mechanical shutter in the optical train.

2. Another solution is to use a liquid crystal shutter, but these have poor throughput at their current state of development [Gaines 1998].
3. A solution would be to use a CCD with a very high frame rate, but an array with a kHz frame rate and $(2048)^2$ pixels would generate 4.2 Gbytes/s of data, which is much more than we need. Further, such arrays are somewhat developmental, and switching automatically generates additional electrical noise.
4. The alternative we favor in this report is the Lexitek PAPA device (Appendix III) gated for interval Δt. The Lexitek PAPA detector is a position-sensitive photon-counting focal plane detector offering the highest spacial and temporal resolution commercially available. The PAPA output is a digital stream of pixel coordinates for each detected photon. Each photon position is available nanoseconds after its acquisition, rather than having to wait for an entire frame readout. Since the input for the device is an image intensifier tube, gating at ms intervals and, e.g., 100Hz rates is easy, and does not add noise. Further, so-called GenIII photocathodes are soon to be available in the device, which will give $\eta_e = 55\%$ at $\lambda = 0.55 - 0.85\mu$m instead of the current $\eta_e = 25\%$ (Appendix III).

4.6 Apparent motion

Debris objects will have apparent motion of 0.5 - 3 degrees per second in low Earth orbit. Using the apparent motion to estimate range can give errors of order 30% (Appendix IV), so angular rate is a good starting point but far from sufficient.

4.7 Atmospheric drag and reacquisition uncertainty

Appendix IV provides detailed information on orbit lifetime τ vs. altitude, eccentricity and area to mass ratio A/m. Kessler, 1978 developed a model for A/m that can be extended into the size range of debris to estimate lifetimes. Lifetime is an important element for estimating nongravitational effects on orbit predictability, as shown in Table 10.

Table 10. Reacquisition uncertainty for likely debris due to atmospheric drag

Diameter d (cm)	Perigee altitude (km)	Eccentricity e	A/m (cm^2/g)	Lifetime (days)	Δt/day (s)	Δx, Δy /day (km)	$d\theta$/day (mrad)
1	200	0	0.3	0.5	———	———	
1	200	0	3.0	0.05	———	———	
1	200	0.05	3.0	3.3	———	———	
10	200	0	0.03	5.0	———	———	
1	500	0	0.3	330	23	175	350
1	500	0	3.0	33	230	1750	3500
1	500	0.05	3.0	1000	7.5	55	110
10	500	0	0.03	3300	2.3	17	34
1	1000	0	0.3	6.7E5	0.024	0.17	0.17
1	1000	0	3.0	6.7E4	0.24	1.7	1.7
1	1000	0.05	3.0	1.3E5	0.12	0.89	0.89
10	1000	0	0.03	6.7E6	0.002	0.017	0.017

Above 500km altitude, the uncertainty due to atmospheric drag is not so large as to prevent reacquiring objects on the following day, provided that a good orbit was determined the first time.

Orbit ephemeris propagation models are another question: but if NORAD elements are accurate to 5 - 15 arc minutes (1.5 – 4 mrad) per day along the orbit [Pohle, 1998], sun-synchronous objects should still be within the FOV of the 32mrad acquisition sensor we propose a day later.

4.8 Active Acquisition Alternative (Haystack radar example)

The principal disadvantage of any form of active acquisition – compared to the passive, solar-illuminated case which we recommend – is that the 32-km-diameter circle we need to illuminate for active acquisition at 1000 km range (in our example) is already flooded with 1 TW of solar flux.

It's hard to do better than that!

Among existing radars, restrictions on elevation or sensitivity mean that only pencil-beam radars, such as the MIT-LL Haystack radar, can see objects smaller than 5cm at 1000 km.

Haystack has done acquisition by staring and has generated most of the data we currently have on 1 – 10-cm debris, working over several years on a contract managed by NASA/JSC. MIT/LL have seen as much as 1.2 acquisitions per hour when they access a debris stream. Since we have shown previously that, on the average, Haystack should see 0.18 acquisitions per hour, the ratio of about 7 provides a good estimate of density variability with time and celestial coordinates.

However, a passive optical system can do it better. In staring mode, good data rate needs bigger field of view than a pencil-beam radar can achieve. If the RF feed in Haystack could be moved to give a larger field of view, then the sensitivity would be bad (see Table 11).

We conclude that the passive visible optical approach is best for acquisition. Passive optical acquisition is also probably cheapest, and most adaptable to high data rates.

Table 11. Passive, Visible optical vs. microwave acquisition

Parameter	AEOS telescope & VIS-λ array	Haystack (36-m aperture) [Hogge & Spencer,1998]
Field of view (optical mods required)	32 mrad	1 mrad
Average acquisition rate for this field of regard	14/hour	0.18/hour
Largest reported acquisition rate	—	1.2/hour
Minimum target @ 1000 km (robust acquisition scenario)	0.7 cm	1 cm
Minimum detectable target @ 1000 km if Haystack modified for 32 mrad FOV	—	30 cm
Operability	3 hours/day	day or night
Operation Cost	?	1.5k$/hour
Handoff circle	13 m	140 m

5. Handoff, Reacquisition and Tracking with HICLASS

5.1 Robust Criteria for Tracking

Active systems are best for tracking, not acquisition. The HICLASS laser, combined with a suitable telescope, is an excellent tracker, potentially much better than radar.

Handoff is recommended to be from passive visible optical to active IR optical.

We take the following two criteria to find robust solutions for tracking with HICLASS. One of these is more robust than for acquisition because we can afford it: acquisition is more difficult than tracking.

Tracking Criterion 1. Robust false alarm rate requires SBR ≈ 100.

Tracking Criterion 2. Robust carrier-to-noise ratio (CNR>12dB) requires N_{pe} ≥15.

Figure 5 shows the minimum signal relationships for this problem. If AEOS were used in conjunction with HICLASS, this can be done for targets bigger than 1.4 mm at 1000 km within a 13m handoff circle, giving 500 photons per kJ, or 15 photons per pulse. QE = 1 in this configuration. This is a very encouraging result for HICLASS. On the other extreme, the combination of LBD and HICLASS could only track 5-cm objects with the above criteria.

This case is different from acquisition in three ways. First, the sensor is already chasing the target because acquisition has told it where to look, so there is no streak, and all the signal photons land on the detector. Second, there is an additional variable in the problem: the laser source energy. This makes the situation even more complex.

Third, there is higher background in the infrared [see Table 5], but it is more than offset by the very large out-of-band rejection ratio ρ = 1E5 (50dB) of the HICLASS heterodyne receiver.

SBR is given by (W = 30J per pulse):

$$\frac{SBR}{pulse} = \frac{W\, c\, T\, \rho}{2\, z\, \lambda_{\mu m}\, B_{\lambda}} \left(\frac{d\sqrt{R}}{d_{sp}}\right)^2 \quad . \qquad [5]$$

Number of photons returned per pulse (equal to N_{pe} since for HICLASS quantum efficiency is ≈1) is

$$\frac{N_{pe}}{pulse} = \frac{W\, T^2\, \eta_e}{4hc/\lambda} \frac{\left(D_b\, d\sqrt{R}\right)^2}{(d_{sp}\, z)^2} \quad . \qquad [6]$$

The problem is still dominated by the same parameters, $D_b d\sqrt{R}$ and $d\sqrt{R}$, but it is best this time to use a specialized diagram to show the degrees of freedom involved [Figure 5] in calculating N_{pe}, in order to avoid plotting a million different graphs for each situation.

Figure 6 shows how tracking SBR depends on d_{sp} using four examples for aperture sizes of the HICLASS beam director. It will almost always be found that tracking SBR is not a problem under conditions discussed here.

Textron calculations for geostationary orbit give a minimum detectable target size in good agreement with the above when range is scaled from 35,882 km to 1000 km.

5.2 Range and range rate resolution

HICLASS can deliver 20cm range resolution, 33cm/s range rate resolution. That doppler resolution corresponds to about 18kHz heterodyne stability for the CO_2 signal. Range rate for actual targets can easily be ±1km/s for targets within a 15° zenith angle cone, or 300 times the receiver bandwidth. Fortunately, the data [Stansbery 1996 Figure 3.3.5] suggests that, if we look straight up, there will always be a clustering of particles with nearly-circular orbits and small range rate, so that a percent or so will be within the bandwidth. A few parallel receiver channels tuned to adjacent frequencies would

help. Considering the 2 seconds or so during which an individual target will be within the FOV of the staring acquisition sensor, an additional tracking technique could be (depending on technical difficulty) stepping the local oscillator through a series of frequencies while tracking the coordinates generated by the acquisition sensor.

5.3 Handoff and Tracking

Procedure:

- The acquisition device identifies a debris track and locates it to within one acquisition pixel as well as predicting its vector in angle space. These coordinates are handed off to the HICLASS tracker.
- Range information is so far absent, but is necessary to correct HICLASS pointing in a significantly bistatic situation. Range can be estimated from angle rate to within 30% in many cases [Appendix IV]. Just from the point of view of calculating pointing angles, if the tracking device is LBD & HICLASS and range is 1000km, the situation is monostatic if the two stations are up to 40m apart, but no further.
- However, any separation at all between acquisition and tracking telescopes will produce uncorrelated tilt components of atmospheric scintillation which will degrade handoff, which were beyond the scope of this study. See "Future Work".
- It is not anticipated that HICLASS do an angle search for the object. The coordinates it is given must be sufficiently accurate for reacquisition *a priori* . Otherwise, the N_{pe} and SBR values we have calculated are far too optimistic.
- Pointing at the right spot in space, and making a final "point-ahead" correction for relativistic effects based on the target velocity vector, HICLASS scans its local oscillator and/or uses parallel demodulation channels to find the target in range-rate space.
- After reacquisition by HICLASS, data which might be collected are: target location within a few meters, range within 20 cm, rate of position, optical cross-section (OCS) versus time (tumbling rate) and OCS vs. polarization and incidence angle (identify the target material via ellipsometry [Azzam and Bashara 1996])
- First-time deductions which might be made from the data include but are not limited to: the composition of the debris population, more accurate determination of the flux and its dependence on inclination, more accurate assessment of maximum to average flux ratio, and more accurate assessment of the true hazard to the Space Station.
- Ultimately, this can be done all the way out to geostationary orbit.
- For km-size near-Earth objects, one of which passes within the orbit of the Moon each month, composition, spin rate, shape and precise orbits.
- Data collection continues until the target leaves the acquisition FOV.

We do not claim that handoff is completely understood in this analysis. There will be many complexities which were not anticipated, some due to the limits of time available for this study and some which will not be discovered until program execution [See §9].

Table 12 summarizes the results of our tracking analysis. The limiting case is always photon count, not SBR for the interesting cases. A substantial sacrifice in capability is associated with using the LBD. However [§ 7] some interesting first steps may be taken with that configuration.

Table 13 shows that AEOS/HICLASS compares favorably in many ways with microwave tracking. A major reason for this is the single photon counting capability of the HICLASS receiver.

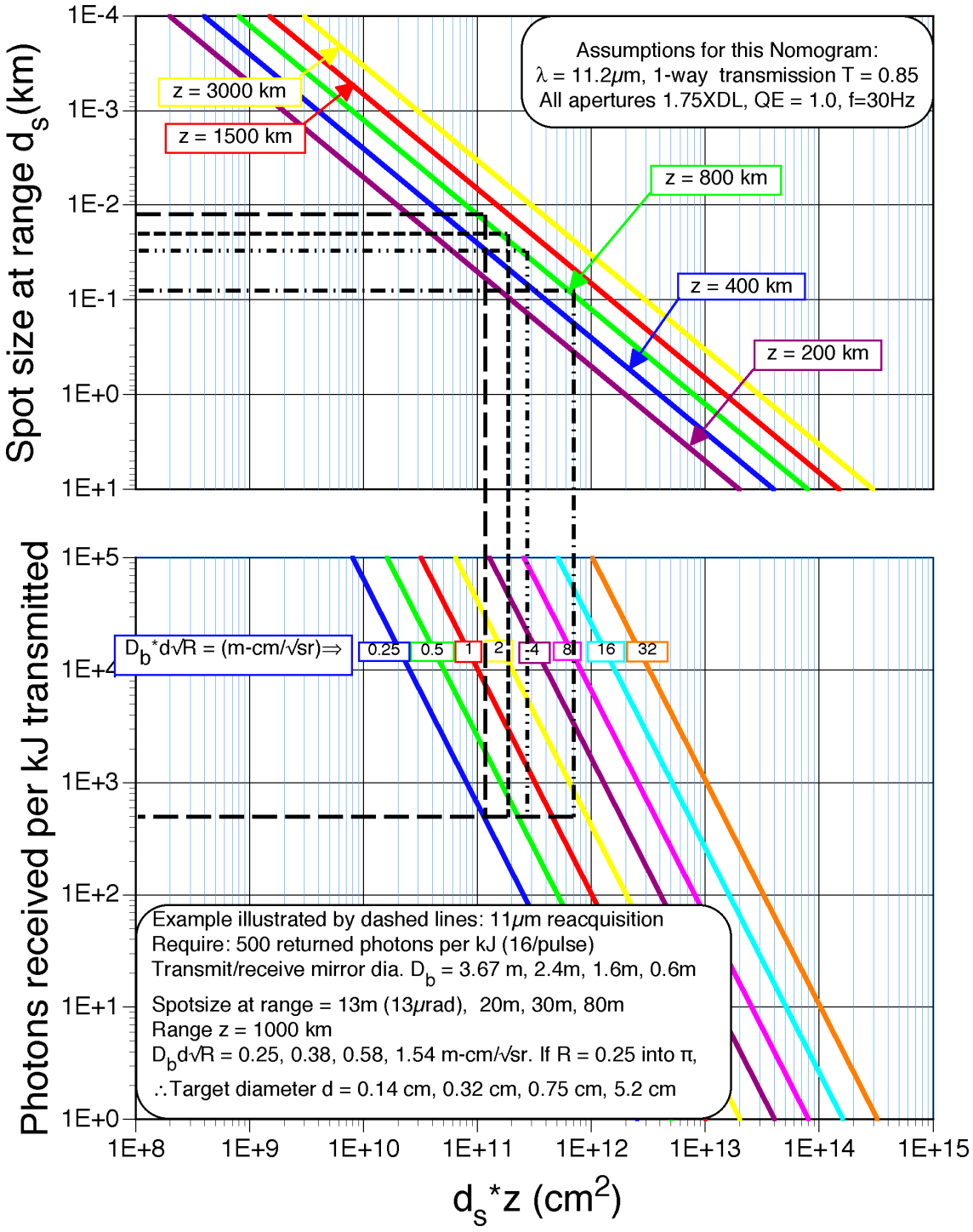

Figure 5. Reacquisition at 11.2μm. Showing how photon count rate depends on other parameters for three aperture diameters launching the HICLASS beam: 3.67m, 2.4m, 1.6m and 60cm (the LBD). The output of the nomogram is the value $D_b d\sqrt{R}$ resulting from inputs of range z, spot size d_s and photons/kJ. Basic assumptions for the nomogram are listed in the box at the top of the Figure. In the example, f=30Hz, W=30J/pulse and range is 1000 km. The heterodyne receiver receives 500 photons/kJ (16 photons/pulse). If diffuse target reflectivity R is 0.25 into π sterradians, debris with diameter d=1.4mm,3.2mm,7.5mm and 5.2cm satisfy the tracking photon-count criterion.

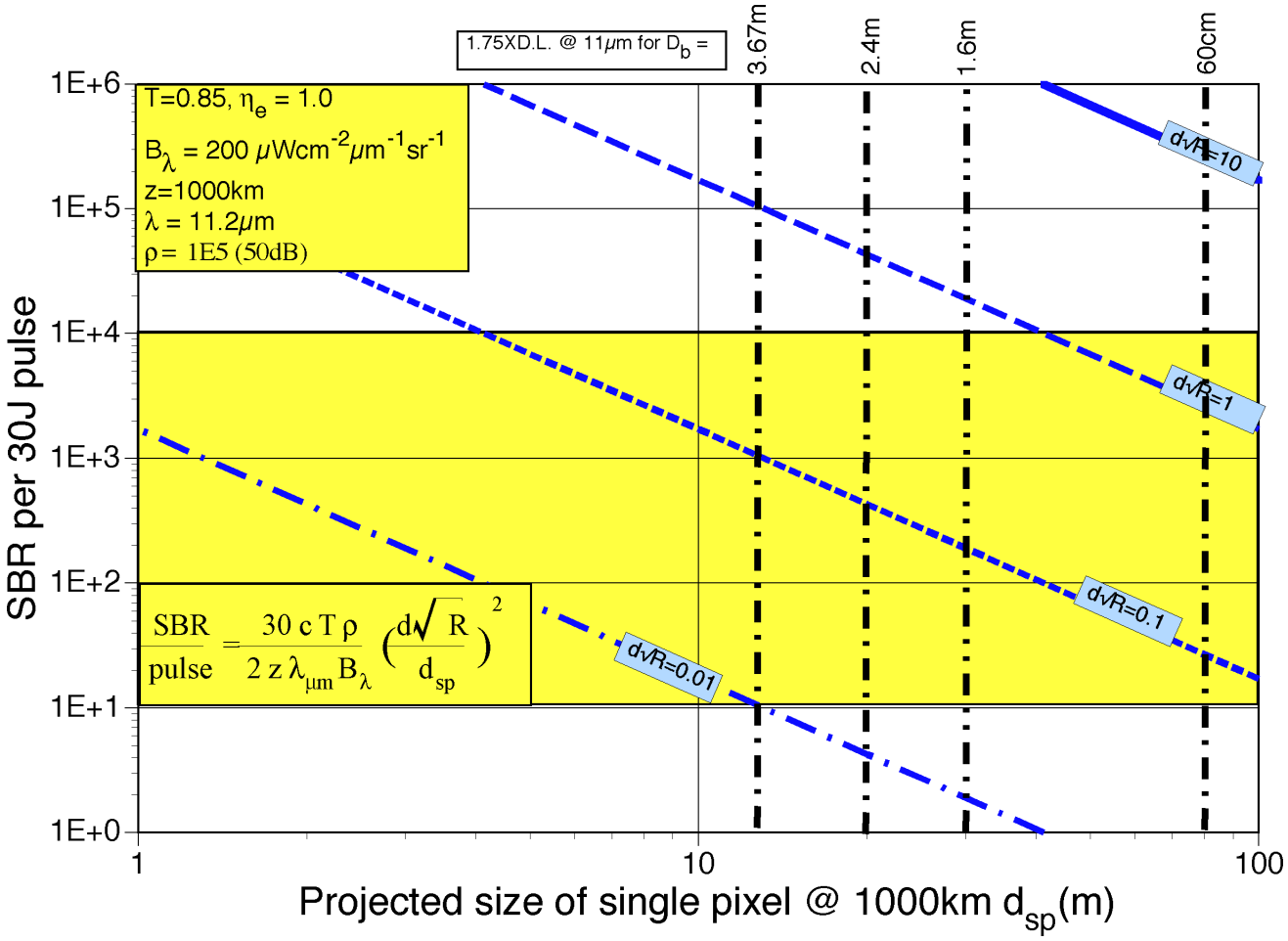

Figure 6. SBR per 30-J HICLASS pulse in tracking mode (blue lines, parameter d√R in cm/√sterrad units) vs. beam footprint diameter at range d_{sp} assuming 100% quantum efficiency, 50dB out-of-band rejection ratio, 85% atmospheric transmission at 1000km range and 11.2μm wavelength. Gold region is desirable. The vertical dashed lines at 13μrad, 20 μrad, 30μrad and 80 μrad represent 1.75 times diffraction limited performance for HICLASS operating with, respectively, the AEOS aperture, the hypothetical telescope having 2.4-m aperture, the 1.6-m telescope at MSSS and the 60-cm LBD.

Table 12. Summary of Results of Figures 5 and 6 for Tracking with HICLASS
[Limiting case (boldface, corresponding to larger result for d) is always N_{pe} for chosen cases; R=0.25]

Criterion: N_{pe} = 15	D_b = 3.67m (AEOS)	D_b = 2.4m (to be built)	D_b=1.6m	D_b=60cm (LBD)
$D_b d\sqrt{R}$ =	0.25	0.38	0.58	1.54
∴ debris size **d =**	**0.14**	**0.32**	**0.75**	**5.2**
Criterion: SBR = 100				
$d\sqrt{R}$ =	0.033	0.050	0.075	0.18
∴ debris size d =	0.07	0.10	0.15	0.36

Table 12 completes our treatment of tracking with HICLASS. It is seen that debris as small as 1.4mm can be tracked at 1000km for moderately bright debris if HICLASS can use AEOS for its beam director. More conclusions based on the Table are listed in §10 of the report.

Table 13. Comparing Best-Case Optical and Microwave Tracking

Parameter	**HICLASS/AEOS**	**HAYSTACK** [Hogge & Spencer, 1998]
Wavelength	11.2 μm	3 cm
Aperture diameter	3.67m	36m
Likely beamwidth	13 μrad	830 μrad
Average power	900W	16 kW
Peak power	3 MW	400 kW
Macropulse duration	3 – 15 μs	1ms
Range resolution	20 cm	25 cm
Doppler resolution	33 cm/s	1 mm/s
Track precision	13 μrad	9 – 18 mrad
Claimed $d\theta/dt$	?	40 mrad/s
Claimed $d^2\theta/dt^2$	?	40 mrad/s^2
Minimum trackable target @ 1000 km	1.4 mm	1 cm

6. Summary: Matching acquisition with tracking

Acquisition must come before tracking. All the previous results can be combined in the following table of examples, which match capabilities for acquisiton and tracking in this multidimensional problem. This is not to say that the smaller aperture should be used for tracking, but just that this is all that is required to match the acquisition capabilitiy listed. Only mirror diameters in Table 12 are considered.

Table 14. Summary of Results of Tables 8 and 12 for Acquisition and Tracking

Debris size d (cm)	Time	R into π	Minimum Acquisition D_b (m)	Minimum Tracking D_b (m)
0.72	Night	0.25	3.67	1.6
2.0	Twilight	0.25	3.67	1.6
0.72	Night	0.25	2.4	1.6
2.0	Twilight	0.25	2.4	1.6
1.0	Night	0.10	3.67	1.6
3.2	Twilight	0.10	3.67	1.6
1.6	Night	0.10	2.4	1.6
3.2	Twilight	0.10	2.4	1.6

Table 15. LWIR results
(Assumed R=1, λ=11.2μm, SBR=2)

FOV d_s (m)	Minimum d (m)
100	8.2
20	1.7
5	0.4

7. LWIR nighttime acquisition

An interesting idea is to use the LWIR radiation of the Earth itself illuminating somewhat larger targets than we have been discussing up to now, to make possible all-night rather than 3-hour-per-day acquisition.

As noted in Table 6, the Earth is a reasonably intense source of radiation. Near-Earth illumination, assuming a 300K blackbody, is $\sigma_{SB}T^4 = 23$ mW/cm^2, equivalent to 0.17 suns peaked at 10.6 μm.

The Planck formula is

$$B_\lambda = 0.001 * \frac{2hc^2}{\lambda^5[\exp\left(\frac{hc}{kT\lambda}\right) - 1]} \ \mathrm{Wcm^{-2}\mu m^{-1}sr^{-1}} \qquad [7]$$

giving 946μWcm^{-2}sr$^{-1}\mu$m^{-1} for Earth as a source in the 11.2 μm region. Background for this case comes mainly from atmospheric LWIR radiation. Using $I_\lambda = 2\pi B_{E\lambda}$ for the Earth as a source [see Table 6, row 1], and denoting by $B_{S\lambda}$ the brightness of the sky background (which – see Table 5 – can be as small as 20 μWcm^{-2}sr$^{-1}\mu$m^{-1} on the best cold night "on the mountain"), Eqn. [7] gives for SBR = 2 and d_s= 5m, d≥ 40 cm as the minimum detectable object using this technique. Other values are listed in Table 15.

In summary, this technique may work for certain situations involving large targets, on the best cold nights at MSSS.

8. Early Demonstration Recommendations

In the following, all costs are very rough order-of-magnitude estimates. Costs for ODERACS insertions may be borne by NASA.

8.1 HICLASS handoff demo proposal #1

Total cost = 175k$ plus manpower.

Best ratio of results to cost.

Targets: One or two d = 5cm ODERACS released by NASA (150k$)

Acquire a relatively large target in the visible with one of the 1-m aperture GEODSS telescopes at Maui and handoff to HICLASS working from the 60-cm LBD. May require fitting GEODSS with upgraded array (20k$), may require gating upgrade (5k$), although image subtraction might be adequate. Spot sizes at 1000km for the two devices are, respectively, d_{s1} = 13m and d_{s2} = 80m, so handoff should be relatively easy, particularly because target range will be known and bistatic angle correction will be straightforward. Targets will have excellent SBR in acquisition and tracking, and just meet the N_{pe} = 15 criterion in tracking [Table 7]. A modified GEODSS should be able to acquire 1 – 3-cm objects at 1000 km in early night, but, because of the LBD's limited aperture, only 5-cm and larger targets can be tracked. Note the bistatic situation, as a minimum, requires dedicated onsite computational capability, and involves additional degradation of handoff from uncorrelated tilt components of atmospheric scintillation which we believe to be acceptable, but which deserve further study.

8.2 HICLASS handoff demo proposal #2

Total cost = 1.1M$ plus manpower costs.

If the budget exists, this is the most scientifically rewarding alternative and, once it is set up, one of the easiest to execute.

Acquisition: Initial tests with a 2.4-m telescope constructed for the purpose at MSSS from low-cost components following a design by Pohle [1998] (250k$). Telescope to be fitted (50k$) with 2048x2048 array, 25% QE (100k$). Tracking: HICLASS beam using the same telescope.

Targets: 10 ODERACS spheres released by NASA on "Getaway Special" at 500km altitude (750k$) plus existing targets of opportunity.

Spot sizes at 1000km for the two devices are, respectively, d_{s1} = 13m and d_{s2} = 80m, so handoff should be relatively easy. Verify the foregoing analyses starting with large, easy targets and working down to the smallest targets that can be acquired.

The bistatic problem does not exist with this option.

Results: Δz = 1m, Δv = 1 m/s, $d\theta$=10μrad $\Rightarrow$ Δx, Δy = 5m, next day: $\approx$ 190 km uncertainty, $\approx$25 s on time of appearance.

8.3 HICLASS tracking signal budget demo at GEO

Total cost = 50k$ plus manpower costs.

Possibly the least complex and least costly of the alternatives to execute because the target is stationary and highest probability of success, but least scientifically interesting.

Target: geostationary satellite with 3.25-m cross-section.

Here, we will need the full AEOS aperture to launch the HICLASS beam. We will require some optical modifications to AEOS (50k$). Pointing direction (the acquisition function) can be computed. At 36 Mm, HICLASS pulse energy density (fluence) will be only Φ=17nJ/cm^2 , peak intensity will be only 1mW/cm^2, and d_s will be 470m. This is well beyond "detector-safe" for the satellite if it has detectors. Assuming R = 0.1 and nighttime, SBR/pulse = 2.3E4, N_{pe}/pulse = 15.

8.4 Related Work at SOR:

In 1997, Phipps observed a one-night campaign at SOR in Albuquerque, the goal of which was to observe debris with a CCD camera using a 14-cm aperture f/2.8 Nikon camera lens. Emphasis was strictly on the USAF cataloged items. During a 10-s exposure at 2230 hours on 22 April 1997, Nimbus IV debris at an altitude of 1000km and range of 1500 km with diameter d = 16 ± 9 cm was detected using frame subtraction.

Referring to Figures 4, we assume $d_s \approx$ 25m at range. It is impossible to know the value of R, but assuming R = 1, $D_b d\sqrt{R} \approx$ 2.2 would have given N_{pe} = 100 and $d\sqrt{R}$ = 16 would have given SBR $\approx$ 3000. These results are consistent with our analysis.

9. Full-up Test Program Recommendation

9.1 We recommend monostatic acquisition and HICLASS tracking using the full AEOS aperture. This eliminates the bistatic problem and gives maximum flexibility to the debris tracking program.

As indicated in Table 14, this choice enables acquisition and tracking of sub-cm debris objects with diffuse reflectivity of at least 10% into π sterradians at night, and 3cm objects in twilight, at 1000km range. Note that this diffuse reflectivity specification is not necessarily equivalent to 20% into 2π. We are describing here what we believe to be realistic parameters for actual debris: 10% diffuse reflectance into a π sterradian cone.

9.2 If the costs and other impact of installing optical components into AEOS which can provide for the necessary ≈2 degree field of view for acquisition and for HICLASS beam insertion are unacceptable, we recommend building a tailored, monostatic, 2.4-m system as suggested by Pohle (1998) to do both acquisition and tracking. As shown in Table 14, the sacrifice in performance will be very slight.

9.3 In both cases, we recommend using the Lexitek gated 2048x2048 PAPA array for acquisition.

10. Conclusions:

Table 14, together with the suggestions for demonstrations outlined in §8, and the full-up program in §9, are the central results of this report.

The purely optical difficulties (photon budget, SBR) for acquisition are more severe than for tracking. If a debris particle can be acquired, it can surely be tracked by HICLASS, operating off any mirror larger than 1.6 meters.

We recommend all-optical, passive, visible wavelength acquisition, combined with infrared HICLASS tracking as the best possible solution for the cost to find and track 1-10-cm debris up to 1000km range.

HICLASS is an excellent tracking device. Somewhat surprisingly, it exceeds, in principle, the performance of tracking radars, since tracking with HICLASS and AEOS can be done for objects down 1.4mm in size. This is because:

Compared to visible wavelength tracking,

- There are 20 times more photons per joule at 11μm, compared to the mid-visible
- There is significantly lower background at MSSS compared to other sites

Compared to radars,

- The viewing solid angle is 4 orders of magnitude smaller and track precision 2 orders of magnitude better
- The HICLASS receiver is capable of single photon counting, about 10 orders of magnitude less than the minimum detectable radar return.

If HICLASS is given adequate information to reacquire a debris object, and it is operating out of either AEOS or a 2.4-m telescope which would be constructed for the tests, it can easily track sub-cm objects. If the budget for the tests is limited and HICLASS is operating off the LBD, then it will not be able to track anything smaller than about 5cm.

ODERACS-type targets could be highly reflective, and would be an interesting contribution from NASA for this project.

LWIR acquisition in Earthlight of objects larger than 40 cm is possible, although the probability of finding one with the necessary small field of view is low.

11. Future Work

Several important aspects still need to be studied by appropriate experts. These include:

- Assess the applicability of frame subtraction, as compared to gating, to achieve good SBR in acquisition.
- Fully analyze the applicability of the RULLI 3D data analysis algorithm (x,y,t) to strongly enhance SBR [see Appendix III].
- Assess the applicability of the RULLI crossed delay line detector in acquisition.
- Complete a detailed engineering analysis of handoff including the impact of mechanical vibration of the mirror mount, relativistic effects, and bistatic location if present.
- Quantify uncorrelated "tilt" aberrations between separated acquisition and tracking sites due to atmospheric scintillation, consider their impact on handoff, and determine their impact on the necessary bandwidth of mechanical and other control systems as well as how to interrogate the tilt and provide the bandwidth.
- Resolve the optical engineering problem associated with obtaining wide acquisition FOV at MSSS. We need 30 mrad.
- Relate the orbit data which will be obtained by the working HICLASS tracking system to making near-real-time density profile measurements of the Earth's atmosphere which are of interest to the USAF.
- Establish optical characterization which can be obtained, including size, shape, reflectivity, orientation, composition and spin. This characterization can be assisted by the well-established results of optical ellipsometry [Azzam and Bashara, 1996].
- Establish the extent to which NASA will work with us on, or help support, this project [ref: ODERACS, USAF/NASA MOA].

References

1. K. Albright, Los Alamos National Lab, private communication (1978)
2. M. Abramowitz and I. Stegun, *Handbook of Mathematical Functions*, NBS Applied Math Series No. 55, USGPO, Washington, 1964, §8.13.5 and §17.3.36
3. AIAA Special Project Report SP-016-1992 *Orbital Debris Mitigation Techniques: Technical, Economic and Legal Aspects* (1992)
4. C. W. Allen, *Astrophysical Quantities*, Athlone Press, London (1973)
5. R.M.A. Azzam and N. M. Bashara, *Ellipsometry and Polarized Light*, North Holland (1996)
6. J. W. Campbell, ed. *Project ORION: Orbital Debris Removal Using Ground-Based Sensors and Lasers*, NASA Marshall Spaceflight Center Technical Memorandum 108522 October 1996
7. H. M. Estes and D. Goldin, USAF Space Command/NASA MOA 2/28/97
8. W. Flury and D. McKnight, *Adv. Space Res.* **13** pp. 299-309 (1993)
9. T. Gaines, SMD Boulder, private communication (1998)
10. H. Goldstein, *Classical Mechanics*, Addison-Wesley, New York (1965)
11. I.S. Gradshteyn and I. M. Ryzhik, *Table of Integrals Series and Products* Academic Press, New York (1965) § 3.664.1
12. V. Hasson, "Long range coherent laser radars for tracking, imaging and chemical detection applications", *Proc. SOQUE Lasers 97*, New Orleans (1977)
13. C. Ho, W. Priedhorsky and M. Baron, in "Space Debris Detection and Mitigation", *Proc. SPIE* **1951** pp. 67 *et seq* (1993)
14. C. B. Hogge and D. B. Spencer, "Orbital Debris and the Environmental Restoration of Space, a report to the Congressional Defense Committees", USAF Research Laboratory report AFRL-VS-PS-TR-1998-1024, February, 1998 and "Orbital Debris Design Study for the Senate Armed Services Committee", USAF Research Lab Memorandum, 30 October, 1997
15. D. J. Kessler, *et al., A computer-based orbital debris environment model for spacecraft design and observation in low Earth orbit* NASA Johnson Spaceflight Center Technical Memorandum 104825 (1996)
16. D. J. Kessler *et al.,* J. Geophys. Res. **83**, 2637 (1978)
17. Desmond King-Hele, *Satellite Orbits in an Atmosphere: Theory and Applications*, Blackie, Glasgow
18. S. R. Maethner, *et al.,* "The Air Force Space Debris Research Program," paper AAS 95-198, AAS/AIAA Spaceflight Mechanics Meeting, Albuquerque (1995)
19. S. R. Maethner, *et al., Report on USAF Space Debris Phase One Study*, PL-TR-94-1042, USAF Phillips Laboratory, June 1994
20. Martin Marietta Technical Report, *Constellation Debris Risk and Mitigation*, October 1994
21. National Research Council, *Orbital Debris, a Technical Assessment*, National Academy Press, Washington (1995)
22. National Science and Technology Council, Office of Science and Technology Policy, *Interagency Report on Orbital Debris 1995,* Washington (1995), Library of Congress 95-72164
23. J. E. Oberg, "Minuteman Third Stage Destroyed by Space Debris," Space News, 2/16/98, pp. 3
24. *Protecting the Space Station from Meteoroids and Orbital Debris*, National Academy Press, Washington (1997)
25. C. R. Phipps, *Project ORION follow-on study for the USAF*, Congressional Debris Language Debris Study Workshop, 28 October 1997

26. C. R. Phipps, H. Friedman, D. Gavel, J. Murray, G. Albrecht, E. V. George, C. Ho, W. Priedhorsky, M. M. Michaelis and J. P. Reilly, "ORION: Clearing near-Earth space debris using a 20-kW, 530-nm, Earth-based, repetitively pulsed laser", *Laser and Particle Beams*, **14** (1) (1996) pp. 1-44

27. R. Pohle, private communication (1998)

28. J. P. Reilly in *Project ORION: Orbital Debris Removal Using Ground-based Sensors and Lasers*, J. W. Campbell, ed., NASA TM 108522, NASA Marshall Spaceflight Center (1996)

29. E. G. Stansbery *et al., Haystack Radar Measurements of the Orbital Debris Environment 1990-1994,* NASA Johnson Spaceflight Center report JSC-27436 (1996)

30. W. L. Wolfe and G. J. Zissis, *The Infrared Handbook*, Office of Naval Research (1978)

Appendix I:

Calculating Acquisition Rate

1. Key physical concepts concerning debris acquisition are:

- **Acquisition rate $\dot{N}$ is linearly proportional to the debris density (number per unit area or solid angle) and to the diameter d_s of the field of view (FOV).**

The number of debris within the FOV is proportional to its area, but the rate at which they enter the FOV is proportional to the FOV perimeter and the velocity with which they cross the perimeter, not the area of the FOV. This is counter-intuitive, but can be understood either dimensionally:

$$\frac{\text{number}}{\text{s}} = \frac{\text{number}}{\text{km}^2}\,\frac{\text{km}}{\text{s}}\,\frac{\text{km}}{1}$$

or by imagining unfolding the FOV perimeter into a straight line segment and counting the rate at which debris cross the line, either due to their own velocity of to the rate at which the line is swept across the sky [see section 2 following].

- **The best sites for Earth-based observation are Equatorial.**

This is because a significant fraction of existing LEO debris have orbits with inclinations to the Equator of 26° or less, corresponding to an Eastward launch from Cape Canaveral.

From Boston, for example (latitude 42°), such objects at the extreme Northward limit of their trajectory and 750 km altitude would appear only 14° above the horizon, involving a sight path through about 4 atmospheres of air.

From Boston, objects which are passing over the Equator at 2200 km altitude directly South of Boston would appear at the horizon, and all the objects at altitudes in which we are interested would be below it.

In contrast, all orbits pass over the Equator.

A temperate-latitude viewing site will never see a large part of the debris population.

- **Though debris exist in density streams which may deviate from the mean density by a factor of 5 or so, uniform distribution is a conservative assumption for analysis.**
- **Though some inclinations are more probable than others, nothing is lost by assuming a random overhead velocity distribution.**
- **To simplify the analysis, we will assume circular orbits for the acquisition rate calculation.**

In particular,
$$v_o = \frac{631.5}{\sqrt{R_E + h}} \text{ km/s} \quad . \qquad \text{[A1.1]}$$

2. A 1-D calculation illustrates most of the principles

[Figure A1] We take a viewpoint at the center of the Earth, and use geocentric angle coordinates (indicated in bold) where, for example

$$\mathbf{d_s} = \frac{d_s}{(R_E + h)} \text{ rad}, \qquad \text{[A1.2]}$$

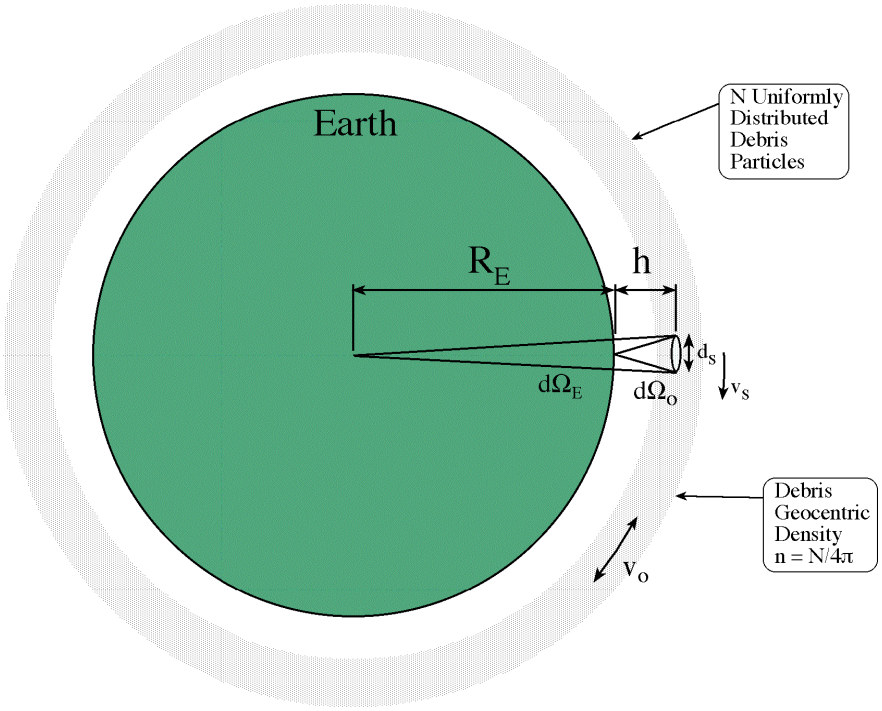

Figure A1.1. Geocentric angle coordinates

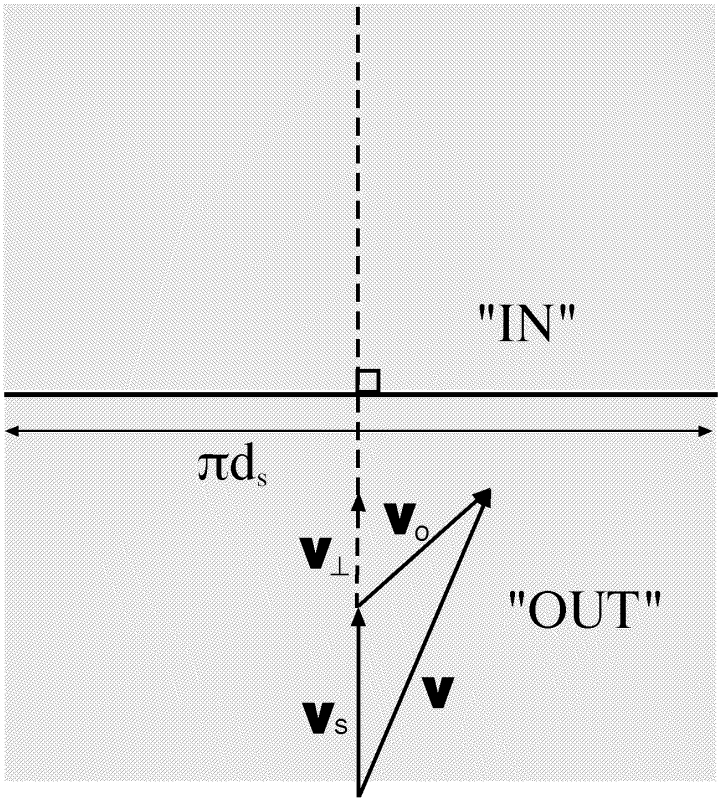

Figure A1.2: Setup for 1-D Calculation

and areal density is

$$\mathbf{n} = \frac{N}{4\pi} \text{ sterrad}^{-1} \qquad [A1.3]$$

for N uniformly distributed debris objects. We now unfold the FOV perimeter into a straight line of length πd_s and imagine it sweeping across the field of density n objects with randomly oriented orbital speed v_o.

From a vantage point on the line slewing with velocity $\mathbf{v_s}$,

$$\mathbf{v}_\perp = \mathbf{v_s} + \mathbf{v_o} \cos\theta \qquad [A1.4]$$

and to pick the "IN's" which are just entering our FOV, we require $v_\perp \geq 0$, which is satisfied for angles $|\theta| < \Theta = \cos^{-1}[-v_s/v_o]$. Integrating over these angles θ, we obtain the 1-D solution:

$$\frac{\dot{N}}{N} = \frac{\mathbf{d_s}}{4}\left[\mathbf{v_s} + \mathbf{v_o}\frac{\sin\Theta}{\Theta}\right] \qquad [A1.5]$$

or, converting back to "real" coordinates,

$$\frac{dN}{dt} = \frac{N\, d_s\, v_o}{4\,(R_E + h)^2}\left[\frac{v_s}{v_o} + \frac{\sin\Theta}{\Theta}\right] . \qquad [A1.6]$$

Eqn. [A1.5] illustrates the basic proportionalities involved (a linear FOV dimension times a velocity), and Eqn. [A6] comes very close to the results for the more accurate 2-D calculation given below. Limits of [A5] are:

$$\frac{\dot{N}}{N}(\text{slewing}) = \frac{\mathbf{d_s v_s}}{4} \qquad [A1.5a]$$

and $$\frac{\dot{N}}{N}(\text{staring}) = \frac{\mathbf{d_s v_o}}{2\pi} . \qquad [A1.5b]$$

3. A 2-D calculation gives more accurate results

[See figure A1.3] In this case, the particle is one of the "IN"'s if

$$\mathbf{v}_{\perp d\ell} = \mathbf{v}\cos\phi > 0, \qquad \text{[A1.6]}$$

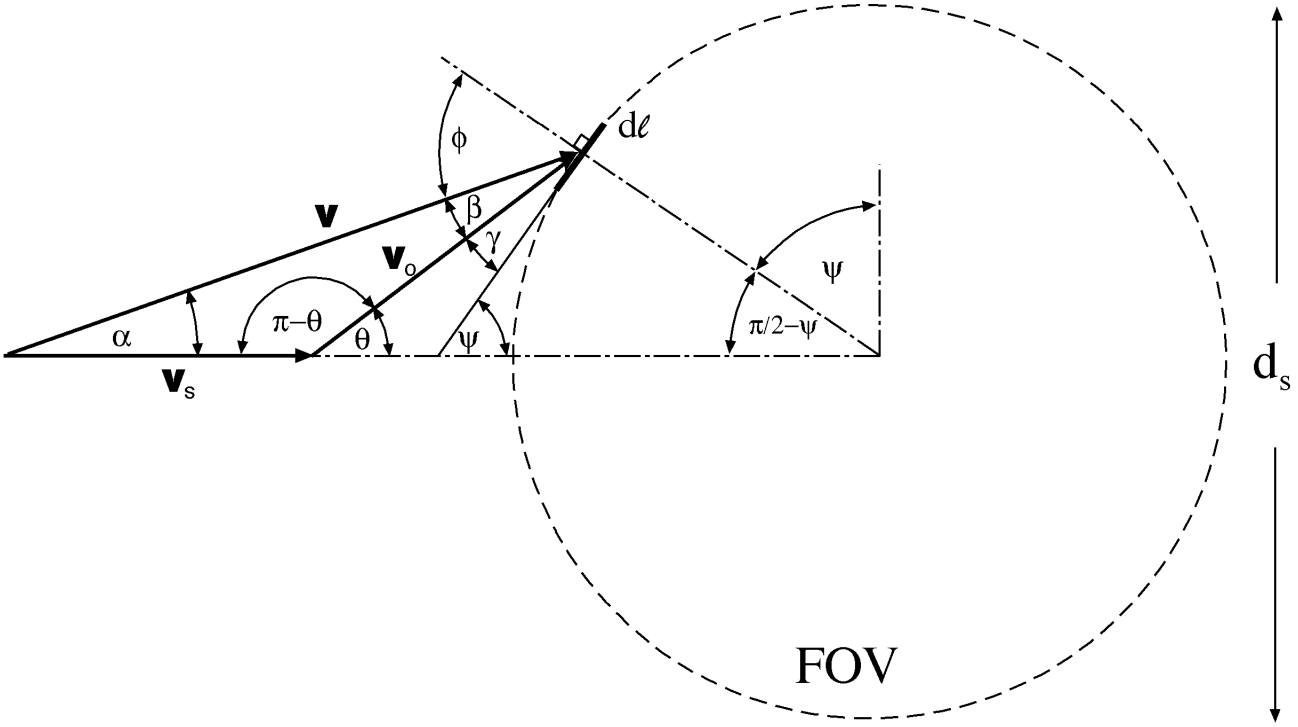

Figure A1.3. Geometry for the Acquisition Rate Calculation

Since
$$\mathbf{v}^2 = \mathbf{v}_s^2 + v_o^2 + 2\,\mathbf{v}_o\,\mathbf{v}_s\cos\theta \qquad \text{[A1.7]}$$

and
$$\beta + \gamma = \psi - \alpha \qquad \text{[A1.8]}$$

the total flux of the "IN"'s is

$$\dot{N} = \oint d\ell\,\cos\phi\; n\,\mathbf{v}_{\perp d\ell} = \frac{N}{2\pi^2}\int_0^{\pi} d\theta\,\mathbf{v}\int_0^{\pi/2} d\phi\,\cos^2\phi \quad . \qquad \text{[A1.9]}$$

With
$$b = \frac{v_o^2 + v_s^2}{2v_o\,v_s} \qquad \text{[A1.10]}$$

the integral
$$I = \frac{1}{\pi}\int_0^{\pi} d\theta\,\mathbf{v} = \frac{\sqrt{2\mathbf{v}_o\mathbf{v}_s}}{\pi}\int_0^{\pi} d\theta\,\sqrt{b+\cos q} \qquad \text{[A1.11]}$$

$$= (z^2-1)^{1/4}\,\pi\,P_{1/2}(z)$$

where $$z = \frac{v_s^2 + v_o^2}{v_s^2 - v_o^2} \quad .$$

Eqn. [A1.11] can be converted to a simpler form for calculations [Gradshteyn & Ryzhik 1965; Abramowitz & Stegun 1964]:

$$\frac{\dot{N}}{N} = \frac{(\mathbf{v}_o + \mathbf{v}_s)\,\mathbf{d}_s}{4\pi}\, E\left[\frac{2\sqrt{\mathbf{v}_o \mathbf{v}_s}}{(\mathbf{v}_o + \mathbf{v}_s)}\right] \quad . \qquad \text{[A1.12]}$$

involving E, the complete elliptic integral of the second kind. Here, the limits are

$$\frac{\dot{N}}{N}(\text{staring}) = \frac{\mathbf{v}_o \mathbf{d}_s}{8} \qquad \text{[A1.12a]}$$

$$\frac{\dot{N}}{N}(\text{slewing}) = \frac{\mathbf{v}_s \mathbf{d}_s}{8} \qquad \text{[A1.12b]}$$

for comparison with the 1-D results [A1.5a] and [A1.5b]. Converting to "real" coordinates,

$$\frac{\dot{N}}{N} = \frac{(v_o + v_s) d_s}{4\pi (R_E + h)^2}\, E\left[\frac{2\sqrt{v_o v_s}}{(v_o + v_s)}\right] \quad . \qquad \text{[A1.12c]}$$

This is the result plotted in Figure 2 of the main text.

Appendix II

Diffuse Reflectivity

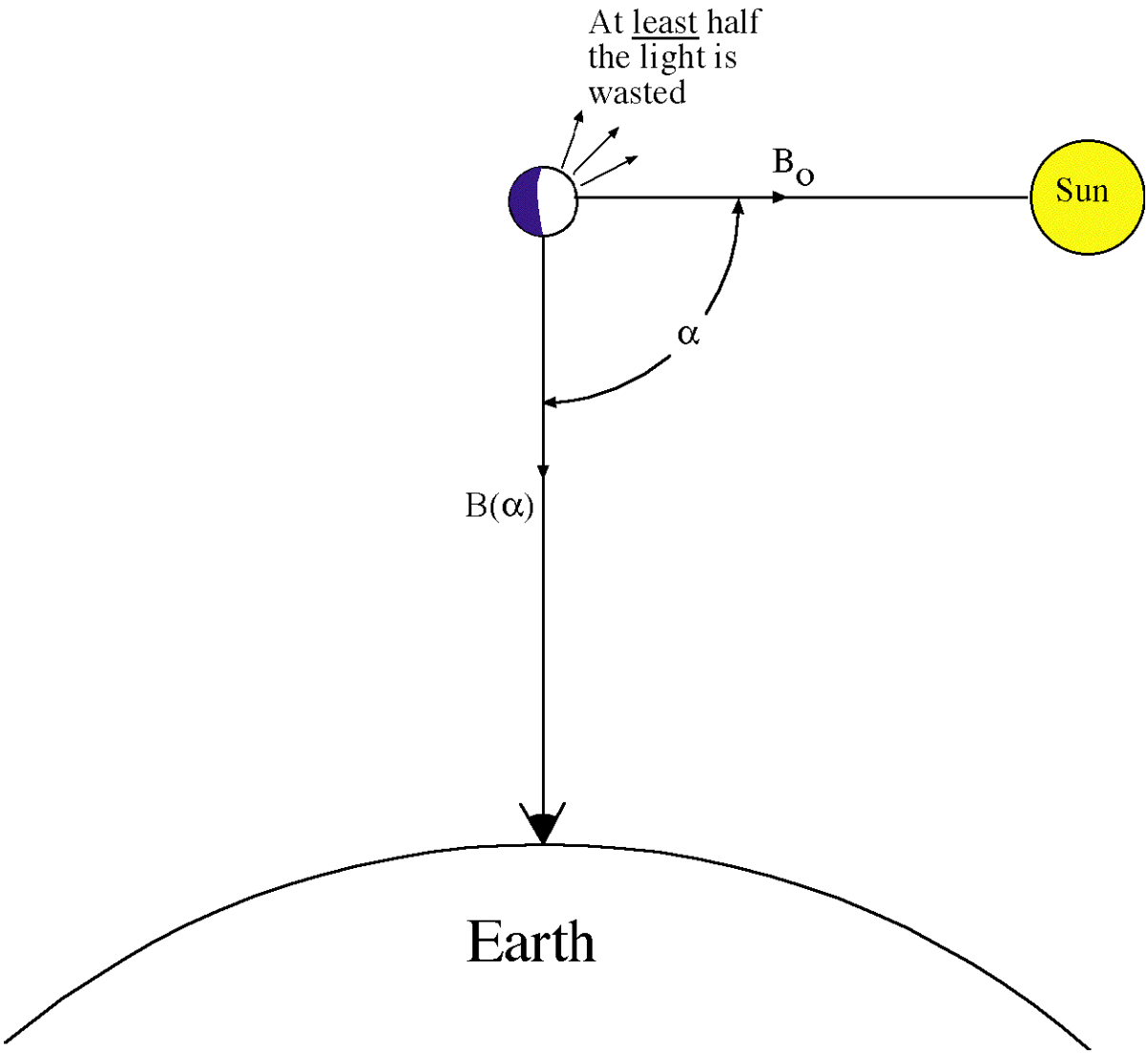

Figure A2.1. Geometry in which most of our targets will be viewed is for scattering angle $\alpha = \pi/2$

Technically [Allen, 1973], where B_{dd} is the on-axis brightness of a perfectly diffusing disk, the "Bond Albedo"

$$R_b = 2\int_0^{\pi} \frac{B(\alpha)}{B_{dd}} \sin\alpha \, d\alpha = \frac{\text{Totallight reflected froma sphere}}{\text{Totallight incident on asphere}} \quad . \qquad [A2.1]$$

Loosely, it can be thought of as reflectivity into π sterradians, since a Lambertian disk at perpendicular incidence with on-axis brightness B_o has total integrated scatter $B_o\pi$.

In this work, we define $R = B(\pi/2)$ = constant over π sterradians. The value chosen obviously depends on the angle α, as indicated in Figures A2.1 and A2.2.

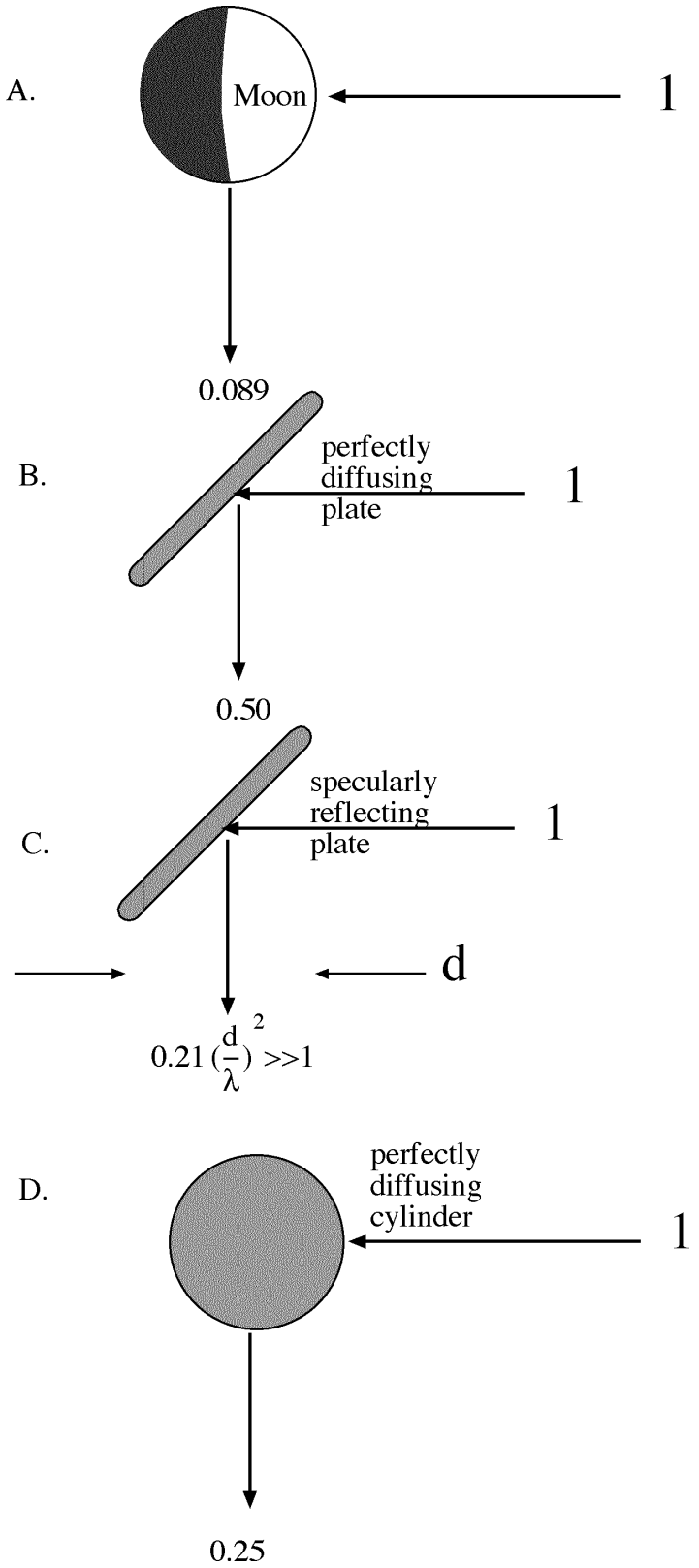

Figure A2.2. Some practical scattering cases

Considering our total uncertainty as to the nature of the debris, and the range of cases illustrated in Figure A2.2, we take R = 0.25 over π sterradians as the baseline condition in this report. As often indicated throughout, it is also clear that (case C) R can be >>1.

Because of the definition, RI_λ/π has the same dimensions as B_λ, $Wcm^{-2}sr^{-1}$.

Appendix III: Sensors & Star Background

Table A3.1 Full Frame Cameras

Mfr	Pixels (HxV)	Pixel Size	Sensor	Features	QE (%)	Frame/s	Approx Cost
Photometrics	2048x2048	9μm	Kodak KAF-4200 CCD	On-chip binning	45	0.13	$50k
EGG Reticon	2048x2048	14	CCD	100dB dynamic range	——	50	——
SMD 4M15	2048x2048	14	Thomson TH7899M CCD	60dB dynamic range	40	15	$25k
Lexitek PAPA	2048x2048	12μm	Intensifier	Gating	25	——	$100k
Lexitek developmental	2048x2048	12μm	ITT GenIII GaAs Ultra Blue Intensifier	Gating	50 (540-840nm)	——	$100k

The Lexitek "PAPA" detector differs from the other 3 listed in that it is a position-sensitive, photon-counting focal plane detector. It offers the highest spacial and temporal resolution commercially available at the present time. The PAPA output is a digital stream of pixel coordinates for each detected photon, rather than a stream of voltage values in a "bucket brigade". Each photon position is available nanoseconds after its detection, and, for this reason, frame rate *per se* is not meaningful.

Because the input device is an image intensifier tube, gating is straightforward and does not increase noise. Gate rates of 10kHz are possible, and gate width can be as little as 150ns, much shorter than we require.

Gating is crucial to our visible acquisition scheme.

The developmental Lexitek camera will use the new ITT "GenIII" tubes, which have 50% quantum efficiency, eliminating the QE penalty of this approach.

For CCD's, a mechanical 1-ms shutter or an intensifier input would be necessary to satisfy the gating requirement.

Statistical Advantage of 3D (x,y,t) Data

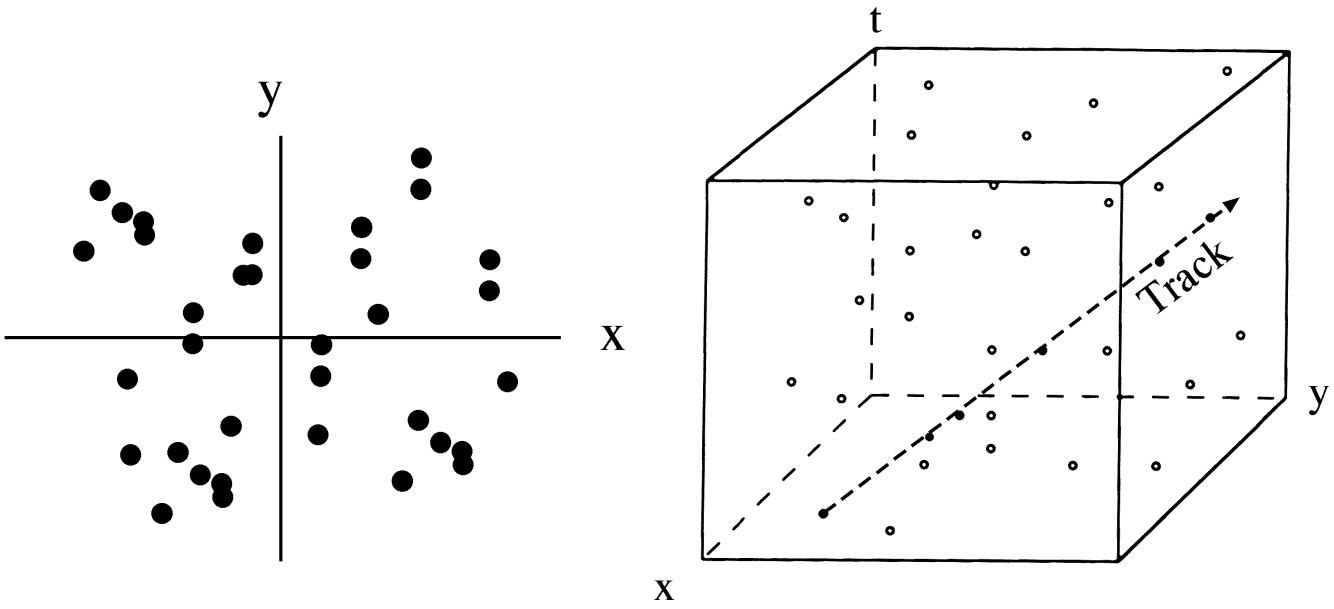

Figure A3.1. Illustrating the statistical advantage of 3D (x,y,t) data representation. The advantage accrues from the fact that the desired target is moving against a fixed background [Ho, *et al* (1993)]

The RULLI sensor developed at Los Alamos (Ho, *et al*, 1993) is also a photon-counting detector. The significance of this program for us (apart from the detector) is the statistical treatment of data permitting a track to be established when SBR<<1.

For background photons randomly distributed in a volume V with density $\rho_{h\nu}$ the mean number of photons contained in a line of length L is

$$<p> = \rho_{h\nu} V_1 \qquad [A3.1]$$

where $V_1 = LS$

is the "volume" of the line, and S its "cross-section". Then, with $N_L(V_1)$ denoting the number of lines with volume V_1 in V, the number of lines of length L consisting of μ photons is

$$N_{L,\mu} = \frac{N_L(V_1)}{\mu!} <p>^{\mu} \exp(-<p>) \qquad [A3.2]$$

The cross-section S of the line can be larger than one square pixel in digitized data, depending on the operational definition of the line.

For example, suppose there are B photons randomly distributed in a grid of $\boldsymbol{D}$ x $\boldsymbol{D}$ pixels. Then, taking $L = \boldsymbol{D}$, S = 1 and $N_L = \boldsymbol{D}^4$, the expected number of lines which could consist of μ photons due to random chance is (false alarm rate)

$$N_{\boldsymbol{D},\mu[3]} \approx \frac{\boldsymbol{D}^4}{\mu!} \left(\frac{B}{\boldsymbol{D}^2}\right)^{\mu} \exp\left(-\frac{B}{\boldsymbol{D}^2}\right) \quad . \qquad [A3.3A]$$

Taking B = 10^6 and $\boldsymbol{D}$ = 2048, we get $N_{\boldsymbol{D},\mu} \leq$ 1E-10 for μ = 16, showing that the detection of a 16-photon line against a background of 10^6 photons is highly significant in the 3D case.

In comparison, if the data is in 2D instead of 3D, the expected number of lines consisting of μ photons due to random chance is

$$N_{\boldsymbol{D},\mu[2]} \approx \frac{\boldsymbol{D}^2}{\mu!} \left(\frac{B}{\boldsymbol{D}}\right)^{\mu} \exp\left(-\frac{B}{\boldsymbol{D}}\right) \quad . \qquad \text{[A3.3B]}$$

With the same parameters, at the same level of significance (1 in 10 billion), we can only hope to find lines consisting of more than about μ = 680 photons. Of these, we expect about 500 photons to come from the background and about 180 from the source. A 16-photon excess would be utterly lost against the background.

In summary, we see a great advantage in going to a 3D data format. To realize this detection scheme, we need a) an imaging photon-counting system with high count rate, and b) a viable data analysis scheme to search for the line.

Star Background

Considering that our debris targets will be 12 to 18th-magnitude, or even higher, it is useful to consider how many stars of the same or greater brightness will be within the approx. 3 square degree FOV. As shown in Figure A3.2, the answer is: several hundred to several thousand, depending on debris magnitude and viewing direction.

This fact alone indicates that the RULLI data processing algorithm will be very important to our success in acquisition.

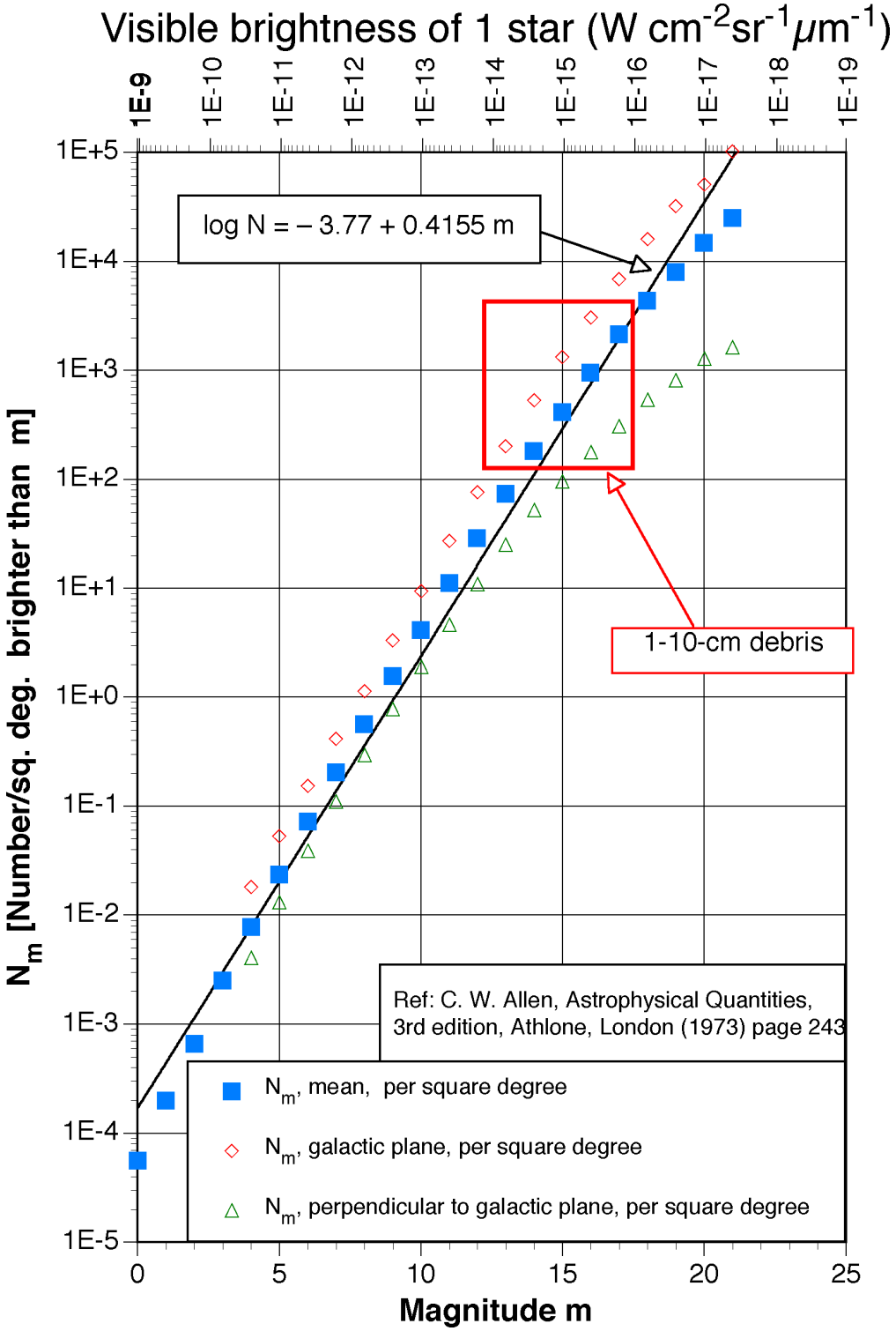

Figure A3.2. Cumulative number density of stars vs. magnitude.

Appendix IV

Apparent Motion as an Altitude Predictor

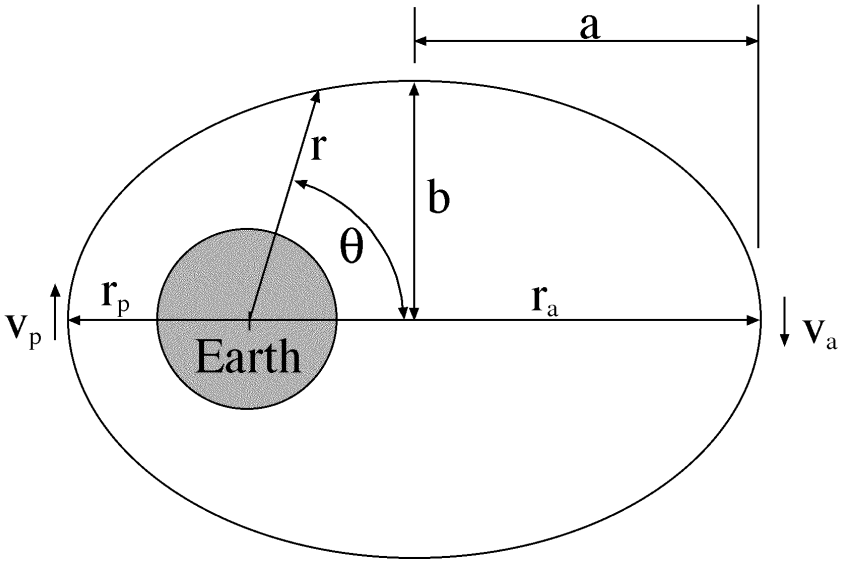

Figure A4.1. Geometry of the orbit problem analyzed here

The apparent motion of an object observed passing overhead, is not a very reliable indicator of its altitude.

We imagine that a family of orbits exist, which have various combinations of apogee and perigee. We wish to determine what we can deduce about the orbit from just one measurement of angular rate of passage.

For the purposes of this analysis, we can ignore nongravitational inputs to the orbit. Angular momentum L is conserved. Other variables are: r, the instantaneous radial vector magnitude; h, the altitude; e, the eccentricity; a, the semi-major axis; b, the semi-minor axis; r_a the apogee radius and r_p the perigee radius of the orbit.

$$\dot{\theta} = \frac{L}{mr^2} \qquad [A4.1]$$

$$L = \sqrt{\frac{GM}{a}}\ bm \qquad [A4.2]$$

$$\frac{b}{a} = \sqrt{1 - e^2} \qquad [A4.3]$$

$$\dot{\theta} = \frac{\sqrt{GMa(1 - e^2)}}{r^2} \qquad [A4.4]$$

$$r_p = a(1 - e) \qquad [A4.5]$$

$$r_a = a(1+e) \qquad [A4.6]$$

$$\dot{\theta} = \frac{1}{r^2}\sqrt{\frac{2GMr_a r_p}{r_a + r_p}} \qquad [A4.7]$$

gives the geocentric angular rate, whereas the observed angular rate from the surface of the Earth is:

$$\text{Angular rate} = \dot{\theta} * (1+R_E/h) \qquad [A4.8]$$

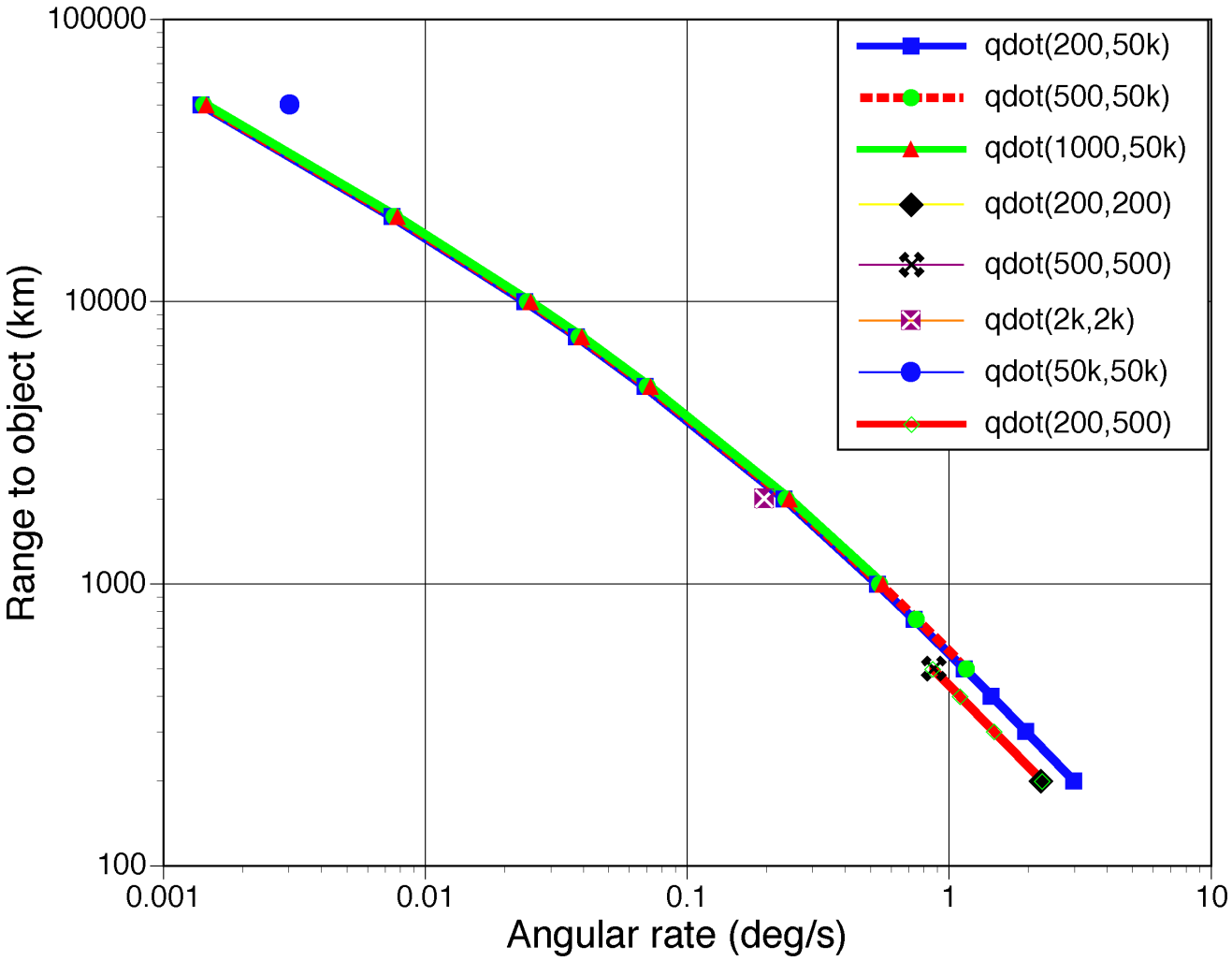

Figure A4.2. Angular rates "qdot" for a family of objects with different orbits (parameters are altitudes) all of which are passing directly overhead. It is seen that the angular rate of 1 deg/s could apply to the objects whose actual range varies from 440km (200x500km orbit) to 570km (500kmx50Mm orbit), giving an uncertainty of 30% for the cases considered. A second case is shown in the Table.

Table A4.1: Possible range for given angular rates

Observed Angular Rate (deg/s)	Range 1 (km)	Orbit 1	Range 2 (km)	Orbit 2	Uncertainty (%)
0.003	33,000	1000x50k	50,000	50kx50k	50
1.0	440	200x500	570	500x50k	30

Lifetime

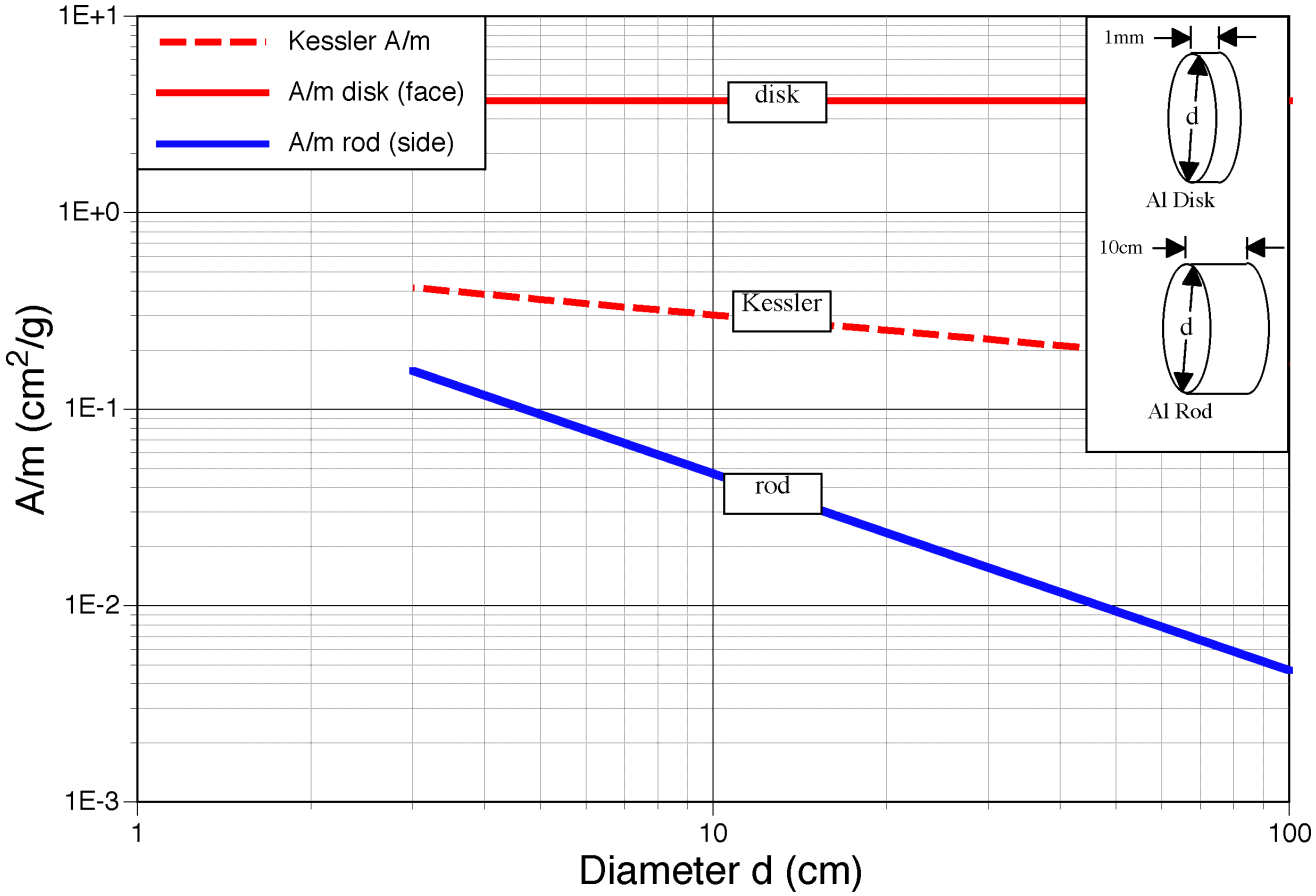

Figure A4.3. Expected range of A/m for debris in the 3-10 cm size range can be estimated from the Kessler model [Kessler and Cour-Palais, J. Geophys. Res. **83**, 2637 (1978)] and from calculations of the ram force.

Where T is orbital period, r the radius and h_o the initial altitude, lifetime is converted into Δt per day as follows:

$$\frac{\Delta r}{(h_o - 100)} = - \frac{\Delta t}{\tau_{life}} \qquad [A4.9]$$

$$\frac{\Delta r}{\Delta t} = - \frac{(h_o - 100)}{\tau_{life}} \qquad [A4.10]$$

$$T = 9.948E{-}3 \; r^{1.5} \; s \qquad [A4.11]$$

$$\frac{\Delta T}{T_o \Delta t} = \frac{1.5 \, \Delta r}{r_o \, \Delta t} \qquad [A4.12]$$

$$r_o = R_E + h_o = 6378 + h_o \qquad [A4.13]$$

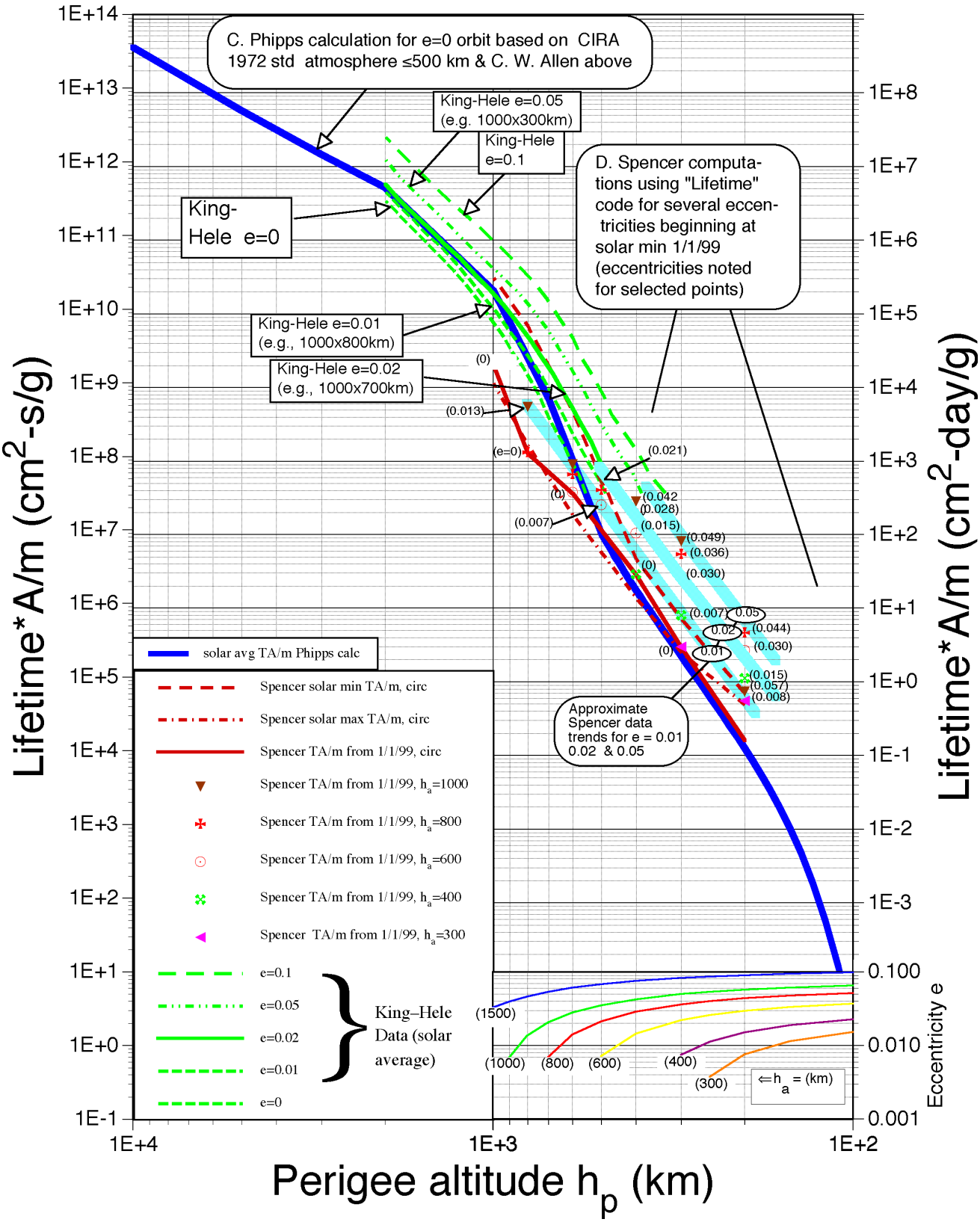

Figure A4.3. Orbital lifetime depends on orbital parameters including perigee height, eccentricity, and A/m, as well as time, since solar flux variations raise and lower the Earth's atmosphere.

$$\frac{1.5\,\Delta r}{r_o} = -\,1.5\,\frac{(h_o - 100)}{(6378+h_o)}\,\frac{\Delta t}{\tau_{life}} = \frac{\Delta T}{T_o} \qquad [A4.14]$$

Where β= apparition time change in seconds per day

$$\beta = \frac{86400}{T}\,\Delta T = \frac{(1.5)(86400)(h_o - 100)}{(6378+h_o)\,\tau_{life(days)}} \qquad [A4.15]$$

Example: τ_{life} = 100 days and h_o = 300km. $\therefore$ β=39s/day; in 100 days.

To get the positional uncertainty $\Delta x = v_o\beta$, we take

$$v_o = \frac{631.5}{\sqrt{R_E + h_o}} \quad \text{km/s} \qquad [A4.16]$$

All this can be put together as shown in the Table.

Table A4.2. Reacquisition uncertainty for likely debris due to atmospheric drag

Diameter d (cm)	Perigee altitude (km)	Eccentricity e	A/m (cm^2/g)	Lifetime (days)	Δt/day (s)	Δx, Δy /day (km)	$d\theta$/day (mrad)
1	200	0	0.3	0.5	———	———	
1	200	0	3.0	0.05	———	———	
1	200	0.05	3.0	3.3	———	———	
10	200	0	0.03	5.0	———	———	
1	500	0	0.3	330	23	175	350
1	500	0	3.0	33	230	1750	3500
1	500	0.05	3.0	1000	7.5	55	110
10	500	0	0.03	3300	2.3	17	34
1	1000	0	0.3	6.7E5	0.024	0.17	0.17
1	1000	0	3.0	6.7E4	0.24	1.7	1.7
1	1000	0.05	3.0	1.3E5	0.12	0.89	0.89
10	1000	0	0.03	6.7E6	0.002	0.017	0.017